Evaluation of global terrestrial evapotranspiration by state-of-the-art approaches in remote sensing, machine learning, and land surface models

Shufen Pan[1], Naiqing Pan[1,2], Hanqin Tian[1], Pierre Friedlingstein[3], Stephen Sitch[4], Hao Shi[1], Vivek K. Arora [5], Vanessa Haverd[6], Atul K. Jain[7], Etsushi Kato[8], Sebastian Lienert[9], Danica Lombardozzi[10], Julia E.M.S. Nabel[11], Catherine Ottlé [12], Benjamin Poulter[13,], Sönke Zaehle[14], Steven W. Running[15]

[1]International Center for Climate and Global Change Research, School of Forestry and Wildlife Sciences, Auburn University, Auburn, AL 36832, USA

[2]State Key Laboratory of Urban and Regional Ecology, Research Center for Eco-Environmental Sciences, Chinese Academy of Sciences, Beijing 100085, China

[3]College of Engineering, Mathematics and Physical Sciences, University of Exeter, Exeter EX4 4QF, United Kingdom

[4]College of Life and Environmental Sciences, University of Exeter, Exeter EX4 4RJ, United Kingdom

[5]Canadian Centre for Climate Modelling and Analysis, Environment Canada, University of Victoria, Victoria, BC, Canada

[6]CSIRO Oceans and Atmosphere, GPO Box 1700, Canberra, ACT 2601, Australia

[7]Department of Atmospheric Sciences, University of Illinois, Urbana, IL 61801, USA

[8]Institute of Applied Energy (IAE), Minato-ku, Tokyo 105-0003, Japan

[9]Climate and Environmental Physics, Physics Institute, University of Bern, Bern, Switzerland

[10]Climate and Global Dynamics Laboratory, National Center for Atmospheric Research, Boulder, CO 80305, USA

[11]Max Planck Institute for Meteorology, Bundesstr. 53, 20146 Hamburg, Germany

[12]LSCE-IPSL-CNRS, Orme des Merisiers, 91191, Gif-sur-Yvette, France
[13]NASA Goddard Space Flight Center, Biospheric Science Laboratory, Greenbelt, MD 20771, USA
[14]Max Planck Institute for Biogeochemistry, P.O. Box 600164, Hans-Knöll-Str. 10, 07745 Jena, Germany
[15]Numerical Terradynamic Simulation Group, College of Forestry & Conservation, University of Montana, Missoula, MT 59812, USA

***Corresponding author**: panshuf@auburn.edu, Tel: 1-334-844-1015

Abstract

Evapotranspiration (ET) is critical in linking global water, carbon and energy cycles. Yet direct measurement of global terrestrial ET is not feasible. Here, we first summarized the basic theory and state-of-the-art approaches for estimating global terrestrial ET, including remote sensing-based physical models, machine learning algorithms and land surface models (LSMs). We then utilized four remote sensing-based physical models, two machine-learning algorithms and fourteen LSMs to analyze the spatial and temporal variations in global terrestrial ET. The results showed that the ensemble means of annual global terrestrial ET estimated by these three categories of approaches agreed well, ranging from 589.6 mm yr^{-1} to 617.1 mm yr^{-1}. For the period 1982-2011, both the ensembles of remote sensing-based physical models and machine-learning algorithms suggested positive trends in global terrestrial ET (0.62 mm yr^{-2} , p<0.05 and 0.38 mm yr^{-2} , p<0.05, respectively). In contrast, the ensemble mean of LSMs showed no statistically significant change (0.23 mm yr^{-2}, p>0.05), even though many of the individual LSMs reproduced a positive trend. Nevertheless, all the twenty models used in this study showed anthropogenic earth greening had a positive role in increasing terrestrial ET. The concurrent small inter-annual variability, i.e. relative stability, found in all estimates of global terrestrial ET, suggests there exists a potential planetary boundary in regulating global terrestrial ET, with the value being about 6.74×10^4 km^3 yr^{-1} (603 mm yr^{-1}). Uncertainties among approaches were identified in specific regions, particularly in the Amazon Basin and arid/semi-arid regions. Improvements in parameterizing water stress and canopy dynamics, utilization of new available satellite retrievals and deep learning methods, and model-data fusion will advance efforts in terrestrial ET estimates.

Keywords: Evapotranspiration; Land surface models; Remote sensing; Machine learning.

1. Introduction

Terrestrial evapotranspiration (ET) is the sum of the water loss to the atmosphere from plant tissues via transpiration and that from the land surface elements including soil, plants and open water bodies through evaporation. Processes controlling ET play a central role in linking the energy (latent heat), water (moisture flux), and carbon cycles (photosynthesis-transpiration trade-off) in the earth system. Over 60% of precipitation on the land surface is returned to the atmosphere through ET (Oki and Kanae, 2006), and the accompanying latent heat (λET, λ is the latent heat of vaporization) accounts for more than half of the solar energy received by the land surface (Trenberth et al., 2009). ET is also coupled with the carbon dioxide exchange between canopy and atmosphere through vegetation photosynthesis. These linkages make ET an important variable in both the short-term numerical weather predication and long-term climate simulations. Moreover, ET is a critical indicator for ecosystem functioning across a variety of spatial scales. For enhancing our predictive understanding of earth system and sustainability, therefore, it is essential to accurately assess land surface ET in a changing global environment.

However, large uncertainty still exists in quantifying the magnitude of global terrestrial ET and its spatial and temporal patterns, despite extensive research (Allen et al., 1998; Liu et al., 2008; Miralles et al., 2016; Mueller et al., 2011; Tian et al., 2010). The previous estimates of global land mean annual ET range from 417 mm yr^{-1} to 650 mm yr^{-1} for the whole or part of the 1982-2011 period (Mu et al., 2007; Mueller et al., 2011; Vinukollu et al., 2011a; Zhang et al., 2010). This large discrepancy among independent studies may be attributed to lack of sufficient measurements, uncertainty in forcing data, inconsistent spatial and temporal resolutions, ill-calibrated model parameters and deficiencies in model structures. Of the four components of ET (transpiration, soil evaporation, canopy interception, and open-water evaporation), transpiration (T_v) contributes the largest uncertainty, as it is modulated not only by surface meteorological conditions and soil moisture but also by the physiology and structures of plants. Changes in non-climatic factors such as elevated atmospheric CO_2, nitrogen deposition, and land covers also serve as influential drivers of T_v (Gedney et al., 2006; Mao et al., 2015; Pan et al., 2018b; Piao et al., 2010). As such, the global ratio of transpiration to ET (T_v/ET) has long been of debate, with the most recent observation-based estimate being 0.64±0.13 constrained by the global water-isotope budget (Good et al., 2015). Most earth system models are thought to largely underestimate T_v/ET (Lian et al., 2018).

Global warming is expected to accelerate the hydrological cycle (Pan et al., 2015). For the period, 1982 to the late 1990s, ET was reported to increase by about 7 mm (~1.2%) per decade driven by an increase in radiative forcing and consequently global and regional temperatures (Douville et al., 2013; Jung et al., 2010; Wang et al., 2010). The contemporary near-surface specific humidity also increased over both land and ocean (Dai, 2006; Simmons et al., 2010; Willett et al., 2007). More recent studies confirmed that, since the 1980s, global ET has showed an overall increase (Mao et al., 2015; Yao et al., 2016; Zeng et al., 2018a; Zeng et al., 2012; Zeng et al., 2016; Zhang et al., 2015; Zhang et al., 2016b). However, the magnitude and spatial distribution of such a trend are far from determined. Over the past 50 years, pan evaporation decreased throughout the world (Fu et al., 2009; Peterson et al., 1995; Roderick and Farquhar, 2002), implying an increase in actual ET given the pan evaporation paradox. Moreover, the increase in global terrestrial ET was found to cease or even be reversed during 1998 to 2008, primarily due to the decreased soil moisture supply in the Southern Hemisphere (Jung et al., 2010). To reconcile the disparity, Douville et al. (2013) argued that the peak ET in 1998 should not be taken as a tipping point because ET was estimated to increase in the multi-decadal evolution. More efforts are needed to understand the spatial and temporal variations of global terrestrial ET and the underlying mechanisms that control its magnitude and variability.

Conventional techniques, such as lysimeter, eddy covariance, large aperture scintillometer and the Bowen ratio method, are capable of providing ET measurements at point and local scales (Wang and Dickinson, 2012). However, it is impossible to directly measure ET at the global scale because dense global coverage by such instruments is not feasible and the representativeness of point-scale measurements to comprehensively represent the spatial heterogeneity of global land surface is also doubtful (Mueller et al., 2011). To address this issue, numerous approaches have been proposed in recent years to estimate global terrestrial ET and these approaches can be divided into three main categories: 1) remote sensing-based physical models, 2) machine learning methods, and 3) land surface models (Miralles et al., 2011; Mueller et al., 2011; Wang and Dickinson, 2012). Knowledge of the uncertainties in global terrestrial ET estimates from different approaches is the prerequisite for future projection and many other applications. In recent years, several studies have compared multiple terrestrial ET estimates (Khan et al., 2018; Mueller et al., 2013; Wartenburger et al., 2018; Zhang et al., 2016b). However, most of these studies analyzed multiple datasets of the same approach or focused on investigating similarities and differences among different approaches. Few studies have been conducted to identify uncertainties in multiple estimates of different approaches.

In this study, we integrate state-of-the-art estimates of global terrestrial ET, including data-driven and process-based estimates, to assess its spatial pattern, inter-annual variability, environmental drivers, long-term trend, and response to vegetation greening. Our goal is not to compare the various models and choose the best one, but to identify the uncertainty sources in each type of estimate and provide suggestions for future model development. In the following sections, we first have a brief introduction to all methodological approaches and ET datasets used in this study. We then quantify the spatiotemporal variations in global terrestrial ET during the period 1982-2011 by analyzing the results from the current state-of-the-art models. Finally, we discuss some suggested solutions for reducing the identified uncertainties.

2. Methodology and data sources

2.1 Overview of approaches to global ET estimation

2.1.1 Remote sensing-based physical models

Satellite remote sensing has been widely recognized as a promising tool to estimate global ET, because it is capable of providing spatially and temporally continuous measurements of critical biophysical parameters affecting ET, including vegetation states, albedo, fraction of absorbed photosynthetically active radiation, land surface temperature and plant functional types (Li et al., 2009). Since the 1980s, a large number of methods have been developed using a variety of satellite observations (Zhang et al., 2016a). However, part of these methods such as surface energy balance (SEB) models and surface temperature-vegetation index (*Ts*-VI) are usually applied at local and regional scales. At the global scales, the vast majority of existing remote sensing-based physical models can be categorized into two groups: the Penman-Monteith (PM) based and the Priestley-Taylor (PT) based models.

A) Remote sensing models based on Penman-Monteith equation

The Penman equation, derived from the Monin-Obukhov similarity theory and surface energy balance, uses surface net radiation, temperature, humidity, wind speed and ground heat flux to estimate ET from an open water surface. For vegetated surfaces, canopy resistance was introduced into the Penman equation by Monteith (Monteith, 1965) and the PM equation is formulated as:

$$\lambda \mathrm{ET} = \frac{\Delta(R_n - G) + \rho_a C_p VPD / r_a}{\Delta + \gamma(1 + {}^{r_s}/_{r_a})} \quad (1)$$

where Δ, R_n, G, ρ_a, C_p, γ, r_s, r_a, VPD are the slope of the curve relating saturated water vapor pressure to air temperature, net radiation, soil heat flux, air density, the specific heat of air, psychrometric constant, surface resistance, aerodynamic resistance and vapor pressure deficit, respectively. The canopy resistance term in the PM equation exerts a strong control on transpiration. For example, based on the algorithm proposed by Cleugh et al. (2007), the MODIS (Moderate Resolution Imaging Spectroradiometer) ET algorithm improved the model performance through inclusion of environmental stress into canopy conductance calculation and explicitly accounted for soil evaporation (Mu et al., 2007). Further, Mu et al. (2011) improved the MODIS ET algorithm by considering nighttime ET, adding soil heat flux calculation, separating dry canopy surface from the wet, and dividing soil surface into saturated wet surface and moist surface. Similarly, Zhang et al. (2010) developed a Jarvis-Stewart-type canopy conductance model based on normalized difference vegetation index (NDVI) to take advantage of the long-term Advanced

Very High Resolution Radiometer (AVHRR) dataset. More recently, this model was improved by adding a CO_2 constraint function in the canopy conductance estimate (Zhang et al., 2015). Another important revision for the PM approach is proposed by Leuning et al. (2008). The Penman-Monteith-Leuning method adopts a simple biophysical model for canopy conductance, which can account for influences of radiation and atmospheric humidity deficit. Additionally, it introduces a simpler soil evaporation algorithm than that proposed by Mu et al. (2007), which potentially makes it attractive to use with remote sensing. However, PM-based models have one intrinsic weakness: temporal upscaling which is required in translating instantaneous ET estimation into a longer time-scale value (Li et al., 2009).This could be easily done at the daily scale under clear-sky conditions but faces challenge at weekly to monthly time-scales due to lack of cloud coverage information.

B) Remote sensing models based on Priestley-Taylor equation

The Priestley–Taylor (PT) equation is a simplification of the PM equation without parameterizing aerodynamic and surface conductance (Priestley and Taylor, 1972) and can be expressed as:

$$\lambda \mathrm{ET} = f_{stress} \times \alpha \times \frac{\Delta}{\Delta+\gamma} \times (R_n - G) \quad (2)$$

where f_{stress} is a stress factor and is usually computed as a function of environmental conditions. α is the PT parameter with a value of 1.2–1.3 under water unstressed conditions and can be estimated using remote sensing. Although the original PT equation works well in estimating potential ET across most surfaces, the Priestley-Taylor coefficient, α, usually needs adjustment to convert potential ET to actual ET (Zhang et al., 2016a). Instead, Fisher et al. (2008) developed a modified PT model that keeps α constant but scales down potential ET by ecophysiological constraints and soil evaporation partitioning. The accuracy of their model has been validated against eddy covariance measurements conducted at a wide range of climates and plant functional types (Fisher et al., 2009; Vinukollu et al., 2011b). Following this idea, Yao et al. (2013) further developed a modified Priestley-Taylor algorithm that constrains soil evaporation using the Apparent Thermal Inertia derived index of soil water deficit. Miralles et al. (2011) also proposed a novel PT type model, Global Land surface Evaporation: the Amsterdam Methodology (GLEAM). GLEAM combines a soil water module, a canopy interception model and a stress module within the PT equation. The key distinguishing features of this model are the use of microwave-derived soil moisture, land surface temperature and vegetation density, and the detailed estimation of rainfall interception loss. In this way, GLEAM minimizes the dependence on static variables, avoids the need for parameter tuning, and enables the quality of the evaporation estimates to rely on the accuracy of the satellite inputs (Miralles et al., 2011). Compared with the PM approach, the PT based approaches avoid the computational complexities of aerodynamic resistance and the accompanying error propagation. However, the many simplifications and semi-empirical parameterization of physical processes in the PT based approaches may lower its accuracy.

2.1.2 Vegetation index-based empirical algorithms and machine learning methods

The principle of empirical ET algorithms is to link observed ET to its controlling environmental factors through various statistical regressions or machine learning algorithms of different complexities. The earliest empirical regression method was proposed by Jackson et al. (1977). At present, the majority of regression models are based on vegetation indices (Glenn et al., 2010), such as NDVI and enhanced vegetation index (EVI), because of their simplicity, resilience in the presence of data gaps, utility under a wide range of conditions and connection with vegetation transpiration capacity (Maselli et al., 2014; Nagler et al., 2005; Yuan et al., 2010). As an alternative to statistical regression methods, machine learning algorithms have been gaining increased attention for ET estimation due to their ability to capture the complex nonlinear relationships between ET and its controlling factors (Dou and Yang, 2018). Many conventional machine learning algorithms, such as artificial neural networks, random forest, and support vector machine based algorithms have been applied in various ecosystems (Antonopoulos et al., 2016; Chen et al., 2014; Feng et al., 2017; Shrestha and Shukla, 2015) and have proved to be more accurate in estimating ET than simple regression models (Antonopoulos et al., 2016; Chen et al., 2014; Kisi et al., 2015; Shrestha and Shukla, 2015; Tabari et al., 2013). In up-scaling FLUXNET ET to the global scale, Jung et al. (2010) used the model tree ensemble method to integrate eddy covariance measurements of ET with satellite remote sensing and surface meteorological data. In a recent study (Bodesheim et al., 2018), the random forest approach was used to derive global ET at a half-hourly time-scale.

2.1.3 Process-based land surface models (LSMs)

Although satellite-derived ET products have provided quantitative investigations of historical terrestrial ET dynamics, they can only cover a limited temporal record of about four decades. To obtain terrestrial ET before 1980s and predict future ET dynamics, LSMs are needed, as they are able to represent a large number of interactions and feedbacks between physical, biological, and biogeochemical processes in a prognostic way (Jimenez et al., 2011). ET simulation in LSMs is regulated by multiple biophysical and physiological properties or processes, including but not limited to stomatal conductance, leaf area, root water uptake, soil water, runoff and sometimes nutrient uptake (Famiglietti and Wood, 1991; Huang et al., 2016; Lawrence et al., 2007). Although almost all current LSMs have these components, different parameterization schemes result in substantial differences in ET estimation (Wartenburger et al., 2018). Therefore, in recent years, the multi-model ensemble approach has become popular in quantifying magnitude, spatiotemporal pattern and uncertainty of global terrestrial ET (Mueller et al., 2011; Wartenburger et al., 2018).

Yao et al. (2017) showed that a simple model averaging method or a Bayesian model averaging method is superior to each individual model in predicting terrestrial ET.

2.2 Description of ET models used in this study

In this study, we evaluate twenty ET products that are based on remote sensing-based physical models, machine-learning algorithms, and LSMs to investigate the magnitudes and spatial patterns of global terrestrial ET over recent decades. Table 1 lists the input data, adopted ET algorithms, limitations, and references for each product. We use a simple model averaging method when calculating the mean value of multiple models.

Four physically-based remote sensing datasets, including Process-based Land Surface Evapotranspiration/Heat Fluxes algorithm (P-LSH), Global Land surface Evaporation: the Amsterdam Methodology (GLEAM), Moderate Resolution Imaging Spectroradiometer (MODIS) and PML-CSIRO (Penman-Monteith-Leuning), and two machine-learning datasets, including Random Forest (RF) and Model Tree Ensemble (MTE), are used in our study. Both machine learning and physical-based remote sensing datasets (totally six datasets) were considered as benchmark products. The ensemble mean of benchmark products was calculated as the mean value of all machine learning and physical-based satellite estimates since we treated each benchmark dataset equally.

Three of the four remote sensing-based physical models quantify ET through PM approaches. P-LSH adopts a modified PM approach coupling with biome-specific canopy conductance determined from NDVI (Zhang et al., 2010). The modified P-LSH model used in this study also accounts for the influences of atmospheric CO_2 concentrations and wind speed on canopy stomatal conductance and aerodynamic conductance (Zhang et al., 2015). MODIS ET model is based on the algorithm proposed by Cleugh et al. (2007). Mu et al. (2007) improved the model performance through the inclusion of environmental stress into canopy conductance calculation, and explicitly accounting for soil evaporation by combing complementary relationship hypothesis with PM equation. The MODIS ET product (MOD16A3) used in this study was further improved by considering night-time ET, simplifying vegetation cover fraction calculation, adding soil heat flux item, dividing saturated wet and moist soil, separating dry and wet canopy, as well as modifying algorithms of aerodynamic resistance, stomatal conductance, and boundary layer resistance (Mu et al., 2011). PML-CSIRO adopts the Penman-Monteith-Leuning algorithm, which calculates surface conductance and canopy conductance by a biophysical model instead of classic empirical models. The maximum stomatal conductance is estimated using the trial-and-error method (Zhang et al., 2016b). Furthermore, for each grid covered by natural vegetation, the PML-CSIRO model constrains ET at the annual scale using the Budyko hydrometeorological model proposed by Fu (1981). GLEAM ET calculation is based on the PT equation, which requires fewer model inputs than PM equation, and the majority of these inputs can be directly achieved from satellite observations. Its rationale is to make the most of information about evaporation contained in the satellite-based environmental and climatic observations (Martens et al., 2017; Miralles et al., 2011). Key variables including air temperature, land surface temperature, precipitation, soil moisture, vegetation optical depth and snow-water equivalent are satellite-observed. Moreover, the extensive usage of microwave remote sensing products in GLEAM ensures the accurate estimation of ET under diverse weather conditions. Here, we use the GLEAM v3.2 version which has overall better quality than previous version (Martens et al., 2017).

The first used machine learning model, MTE, is based on the Tree Induction Algorithm (TRIAL) and Evolving Trees with Random Growth (ERROR) algorithm (Jung et al., 2009). The TRIAL grows model trees from the root node and splits at each node with the criterion of minimizing the sum of squared errors of multiple regressions in both subdomains. ERROR is used to select the model trees that are independent from each other and have best performances under Schwarz criterion. Canopy fraction of absorbed photosynthetic active radiation (fAPAR), temperatures, precipitation, relative humidity, sunshine hours, and potential radiation are used as explanatory variables to train MTE (Jung et al., 2011). The second machine learning model is the random forest (RF) algorithm whose rationale is generating a set of independent regression trees through randomly selecting training samples automatically (Breiman, 2001). Each regression tree is constructed using samples selected by bootstrap sampling method. After fixing individual tree in entity, the final result is determined by simple averaging. One merit of RF algorithm is its capability of handling complicated nonlinear problems and high dimensional data (Xu et al., 2018). For the RF product used in this study, multiple explanatory variables including enhanced vegetation index, fAPAR, leaf area index, daytime and nighttime land surface temperature, incoming radiation, top of atmosphere potential radiation, index of water availability and relative humidity were used to train regression trees (Bodesheim et al., 2018).

The fourteen LSMs-derived ET products were from the Trends and Drivers of the Regional Scale Sources and Sinks of Carbon Dioxide (TRENDY) Project (including CABLE, CLASS-CTEM, CLM45, DLEM, ISAM, JSBACH, JULES, LPJ-GUESS, LPJ-wsl, LPX-Bern, O-CN, ORCHIDEE, ORCHIDEE-MICT and VISIT). Daily gridded meteorological reanalyses from the CRU-NCEPv8 dataset (temperature, precipitation, long- and short-wave incoming radiation, wind-speed, humidity, air pressure) were used to drive the LSMs. The TRENDY simulations were performed in year 2017 and contributed to the Global Carbon Budget reported in Le Quéré et al. (2018). We used the results of S3 experiment of $\mathrm{TRENDY_V6}$ (with changing CO_2, climate and land use) over the period 1982-2011, a time period consistent with other products derived from remote sensing-based physical models and machine-learning algorithms.

2.3 Description of other datasets

To quantify the contributions of vegetation greening to terrestrial ET variations, we used the LAI of TRENDY$_V$6 S3 experiment. We also used the newest version of the Global Inventory Modeling and Mapping Studies LAI data (GIMMS LAI3gV1) as satellite-derived LAI. GIMMS LAI3gV1 was generated from AVHRR GIMMS NDVI3g using an Artificial Neural Network (ANN) derived model (Zhu et al., 2013). It covers the period 1982 to 2016 with bimonthly frequency and has a 1/12° spatial resolution. To achieve a uniform resolution, all data were resampled to 1/2° using the nearest neighbour method. Following Pan et al. (2018a), grids with an annual mean NDVI<0.1 were assumed to be non-vegetated regions and were therefore masked out. NDVI data are from GIMMS NDVI3gV1 dataset. Temperature, precipitation and radiation are from CRU-NCEPv8.

2.4 Statistical analysis

The significance of ET trends is analyzed using the Mann-Kendall (MK) test (Kendall, 1955; Mann, 1945). It is a rank-based non-parametric method that has been widely applied for detecting a trend in hydro-climatic time series (Sayemuzzaman and Jha, 2014; Yue et al., 2002). The Theil-Sen estimator was applied to estimate the magnitude of the slope. The advantage of this method over ordinary least squares estimator is that it limits the influence of the outliers on the slope (Sen, 1968).

Terrestrial ET IAV is mainly controlled by variations in temperature, precipitation, and shortwave solar radiation (Zeng et al., 2018b; Zhang et al., 2015). In this study, we performed partial correlation analyses between ET and these three climatic variables at an annual scale for each grid cell to explore climatic controls on ET IAV. Variability caused by climatic variables was assessed through the square of partial correlation coefficients between ET and temperature, precipitation, and radiation. We chose partial correlation analysis because it can quantify the linkage between ET and a single environmental driving factor while controlling the effects of other remaining environmental factors. Partial correlation analysis is a widely applied statistical tool to isolate the relationship between two variables from the confounding effects of many correlated variables (Anav et al., 2015; Jung et al., 2017; Peng et al., 2013). All variables were first detrended in the statistical correlation analysis since we focus on the inter-annual relationship. The study period is from 1982 to 2011 for all models except MODIS and Rand Forest whose temporal coverage is limited to 2001-2011 because of data availability.

To quantify the contribution of vegetation greening to terrestrial ET, we separated the trend in terrestrial ET into four components induced by climatic variables and vegetation dynamics by establishing a multiple linear regression model between global ET and temperature, precipitation, shortwave radiation, and LAI (Eq. 3-4):

$$\delta(ET) = \frac{\partial(ET)}{\partial(LAI)}\delta(LAI) + \frac{\partial(ET)}{\partial\mathrm{T}}\delta(\mathrm{T}) + \frac{\partial(ET)}{\partial(\mathrm{P})}\delta(\mathrm{P}) + \frac{\partial(ET)}{\partial\mathrm{R}}\delta(\mathrm{R}) + \varepsilon \quad (3)$$

$$\delta(ET) = \gamma_{ET}^{LAI}\delta LAI + \gamma_{ET}^{\mathrm{T}}\delta\mathrm{T} + \gamma_{ET}^{\mathrm{P}}\delta\mathrm{P} + +\gamma_{ET}^{\mathrm{R}}\delta\mathrm{R} + \varepsilon \quad (4)$$

γ_{ET}^{LAI}, γ_{ET}^{T}, γ_{ET}^{P}, γ_{ET}^{R} are the sensitivities of ET to leaf area index (LAI), air temperature (T), precipitation (P), and radiation (R), respectively. ε is the residual, representing the impacts of other factors.

After calculating γ_{ET}^{LAI}, γ_{ET}^{T}, γ_{ET}^{P}, γ_{ET}^{R}, the contribution of trend in factor i ($Trend(i)$) to the trend in ET ($Trend(\mathrm{ET})$) can be quantified as follows:

$$\mathrm{Contri(i)}= (\gamma_{ET}^{i} \times Trend(i))/Trend(\mathrm{ET}) \quad (5)$$

In performing multiple linear regression, we used GIMMS LAI for both remote sensing-based physical models and machine learning methods, and individual TRENDYv6 LAI for each TRENDY model. The gridded data of temperature, precipitation and radiation are from CRU-NCEPv8

3. Results

3.1 The ET magnitude estimated by multiple models

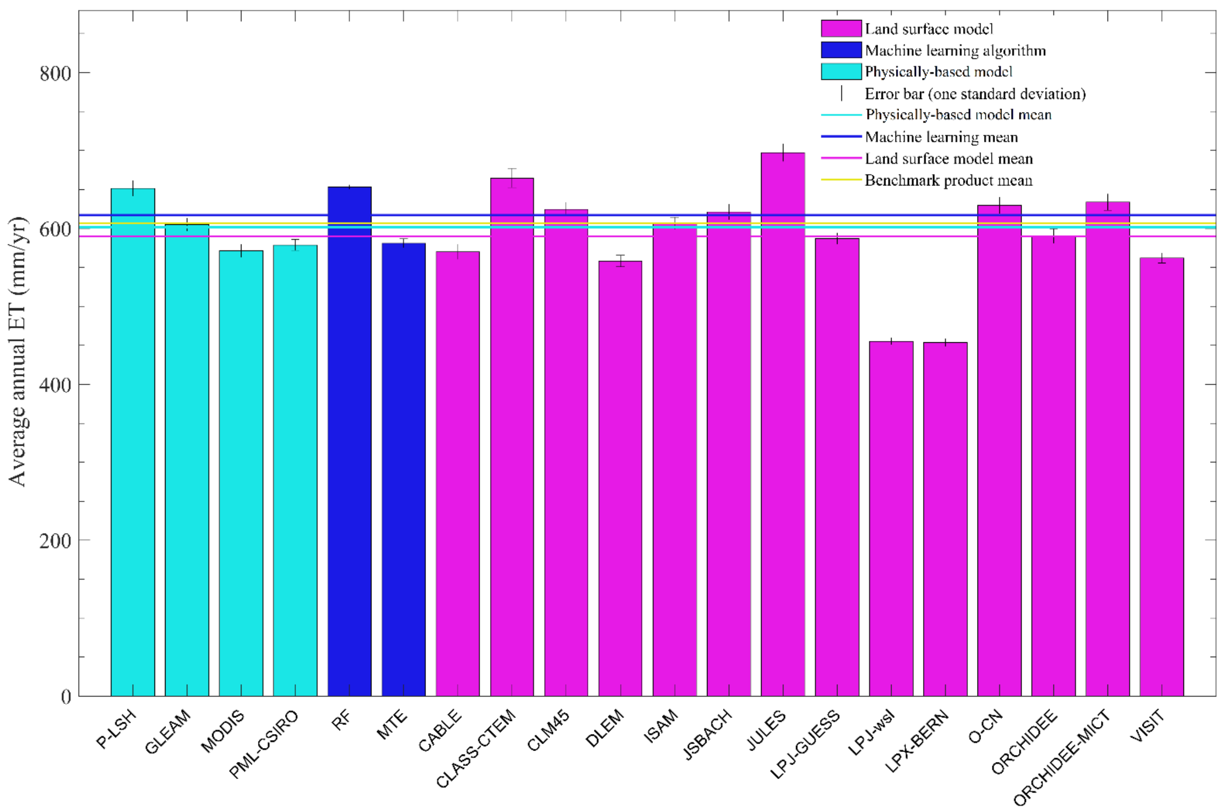

Figure 1. Average annual global terrestrial ET estimated by each model during the period 2001-2011. Error bars represent the standard deviation of each model. The four lines indicate the mean value of each category.

The multi-year ensemble mean of annual global terrestrial ET during 2001-2011 derived by the machine learning methods, remote sensing-based physical models and TRENDY models agreed well, ranging from 589.6 mm yr^{-1} to 617.1 mm yr^{-1}. However, substantial differences existed among individual models (Fig. 1). LPJ-wsl (455.3 mm yr^{-1}) and LPX-Bern (453.7 mm yr^{-1}) estimated significantly lower ET than other models, even in comparison with most previous studies focusing on earlier periods (Table S1). In contrary, JULES gave the largest ET estimate (697.3 mm yr^{-1}, equals to 7.57×10^{4} km^{3} yr^{-1}) among all models, and showed an obvious increase of ET compared to its estimation during 1950-2000 (6.5×10^{4} km^{3} yr^{-1}, Table S1).

3.2 Spatial patterns of global terrestrial ET

As shown in Fig. 2, the spatial patterns of multi-year average annual ET of different categories were similar. ET was the highest in the tropics and low in northern high latitudes and arid regions such as Australia, central Asia, western U.S., and Sahel. Compared to remote sensing-based physical models and LSMs, machine-learning methods obtained a smaller spatial gradient. In general, latitudinal profiles of ET estimated by different approaches were also consistent (Fig. 3). However, machine-learning methods gave higher ET estimate at high latitudes and lower ET in the tropics compared to other approaches. In the tropics, LSMs have significant larger uncertainties than benchmark products, and the standard deviation of LSMs is about two times as large as that of benchmark products (Fig. 3). In other latitudes, LSMs and benchmark ET products have generally comparable uncertainties. The largest difference in ET of different categories was found in the Amazon Basin (Fig. 2). In most regions of the Amazon Basin, the mean ET of remote sensing physical models are more than 200mm yr^{-1} higher than the mean ET of LSMs and machine-learning methods. For individual ET estimates, the largest uncertainty was also found in the Amazon Basin. MODIS, VISIT and CLASS-CTEM estimated that annual ET was larger than 1300 mm in the majority of Amazon, whereas JSBACH and LPJ-wsl estimated ET of smaller than 800 mm yr^{-1} (Fig. S1). As is shown in Fig. S2, the difference in ET estimates among TRENDY models were larger than those among benchmark estimates for tropical and humid regions. The uncertainty of ET estimates by LSMs is particularly large in the Amazon Basin where the standard deviation of LSMs estimates is more than two times as large as that of benchmark estimates. It is noteworthy that, in arid and semi-arid regions such as western Australia, central Asia, northern China and western US, the difference in ET estimates among LSMs is significantly smaller than those among remote sensing models and machine learning algorithms.

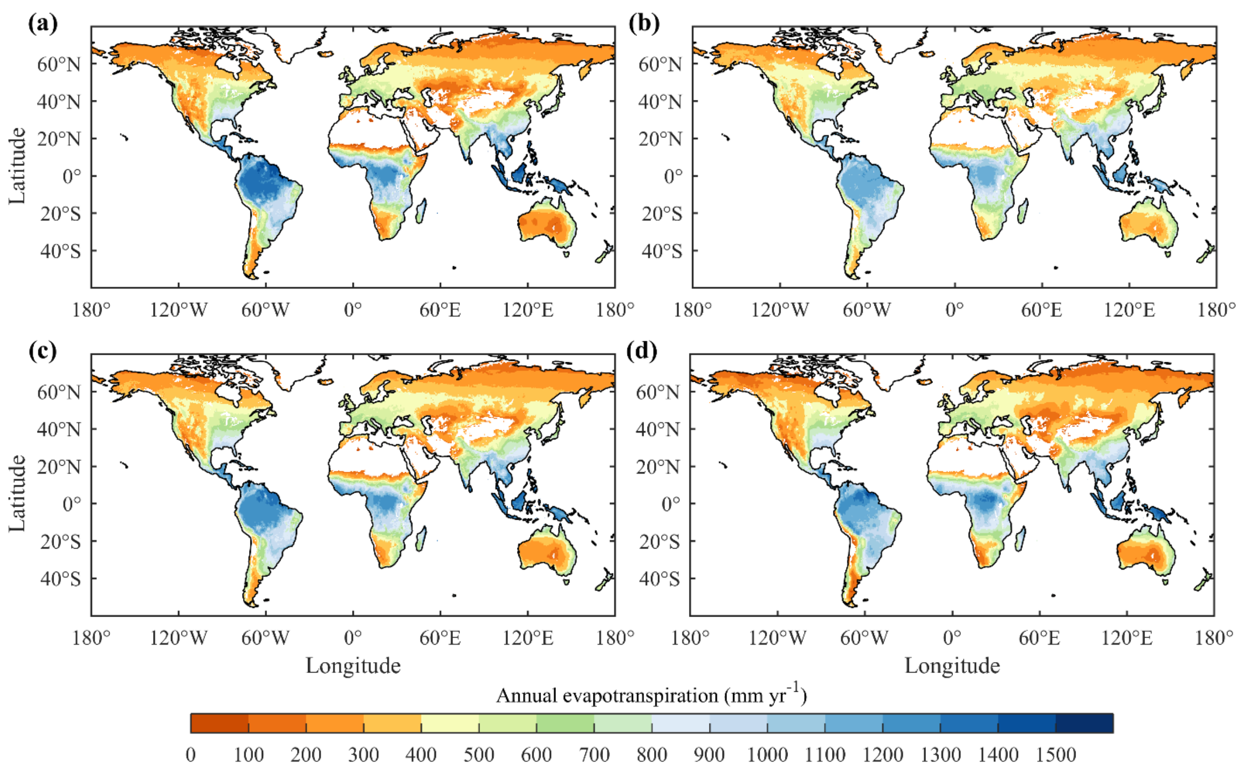

Figure 2. Spatial distributions of mean annual ET derived from (a) remote sensing-based physical models, (b) machine-learning algorithms, (c) benchmark datasets and (d) TRENDY LSMs ensemble mean, respectively.

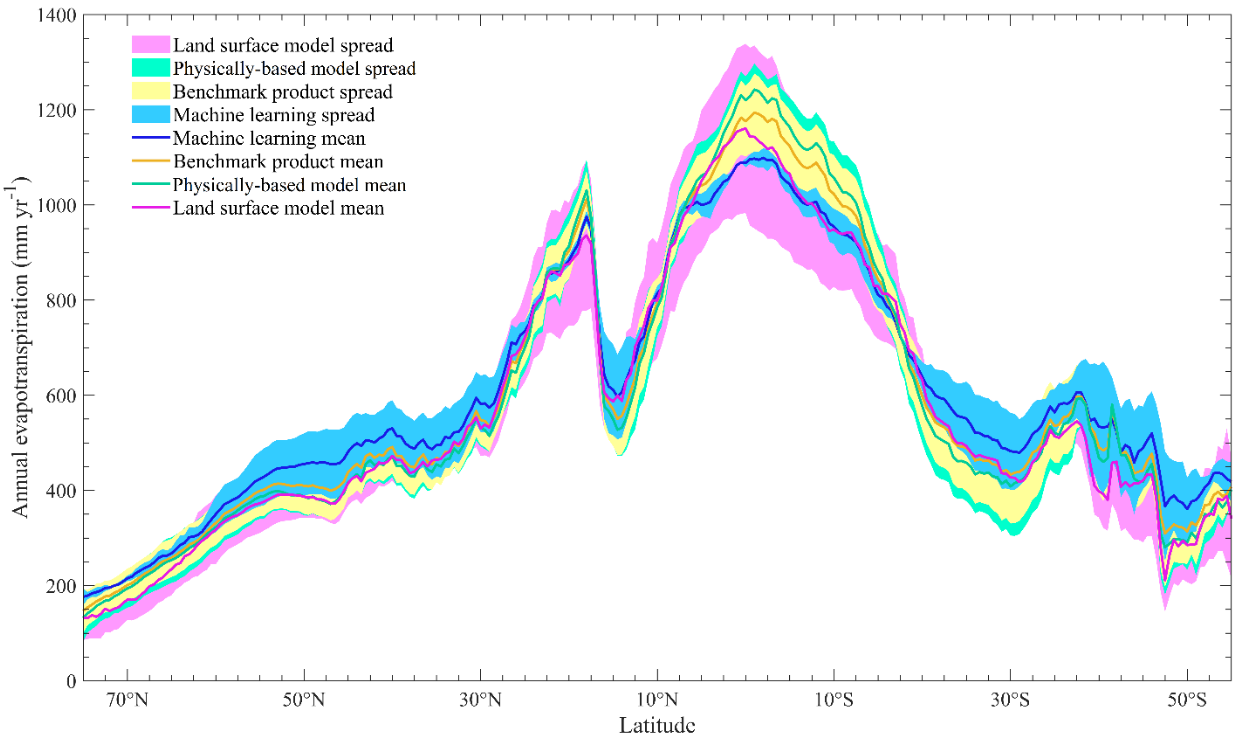

Figure 3. Latitudinal profiles of mean annual ET for different categories of models. Each line represents the mean value of the corresponding category and the shading represents the interval of one standard deviation.

3.3 Inter-annual variations in global terrestrial ET

The ensemble mean inter-annual variability (IAV) of remote sensing ET estimates and LSMs ET estimates showed similar spatial patterns (Fig. 4). Both remote sensing physical models and LSMs presented low IAV in ET in northern high latitudes but high IAV in ET in southwestern U.S, India, south Sahara Africa, Amazon and Australia. In contrast, IAV of machine-learning based ET was much weaker. In most regions, IAV of machine learning ET is smaller than 40% of IAV of remote sensing physical ET and LSMs ET, and this phenomenon is especially pronounced in tropical regions. Further investigation into the spatial patterns of ET IAV for individual model showed that the two machine-learning methods performed equally in estimating spatial patterns of ET IAV

(Fig. S4). In contrast, differences in ET IAV among remote sensing physical estimates and LSMs estimates were much larger. LSMs showed the largest differences in IAV of ET in tropical regions. For example, CABLE and JULES obtained an ET IAV of smaller than 15 mm yr^{-1} in most regions of the Amazon Basin, while LPJ-GUESS predicted an ET IAV of larger than 60 mm yr^{-1}. Figure 5 showed that, in the north of 20ºS, remote sensing physical ET and LSMs ET had comparable IAV, but IAV of the machine learning based ET was much smaller. In the region south of 20ºS, TRENDY ET showed the largest IAV, followed by those of remote sensing physical ET and machine learning estimates. The three approaches agreed on that ET IAV in the Southern Hemisphere was generally larger than that in the Northern Hemisphere.

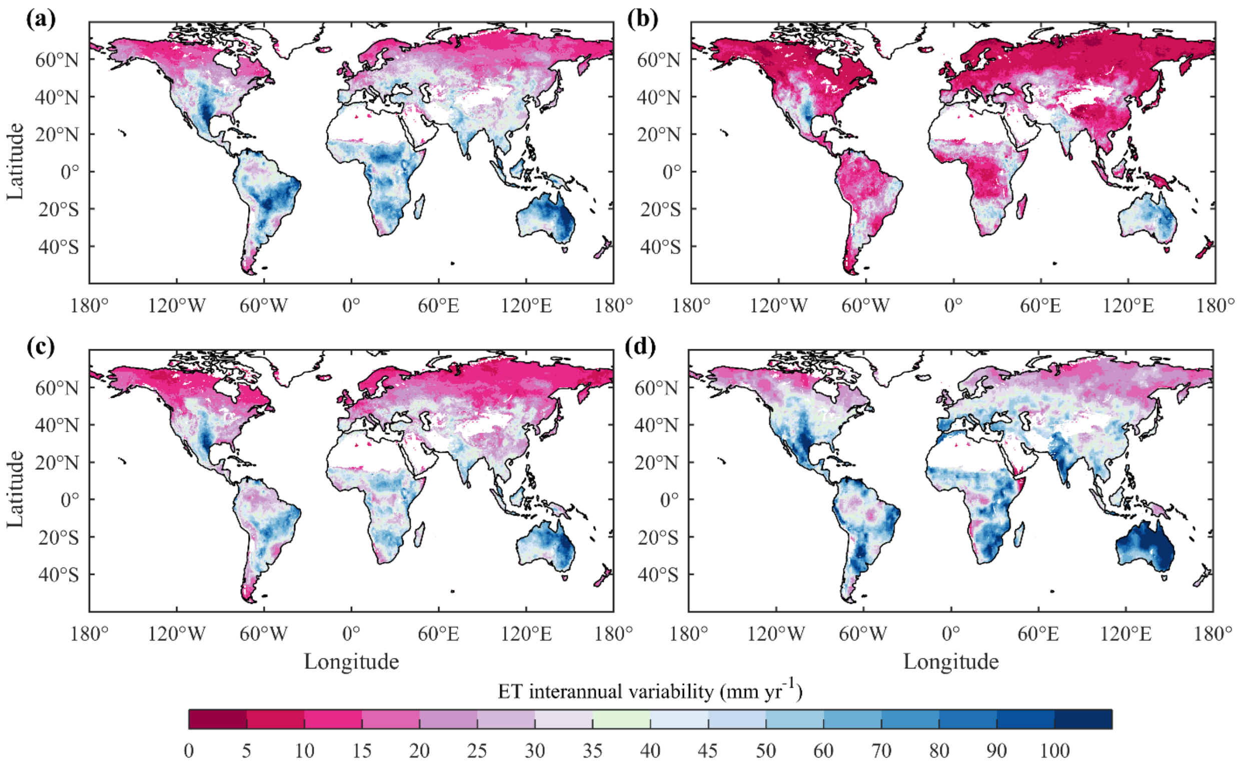

Figure 4. Spatial distributions of the inter-annual variability in ET derived from (a) remote sensing-based physical models, (b) machine learning algorithms, (c) benchmark datasets, and (d)

TRENDY LSMs ensemble mean, respectively. The study period used in this study for inter-annual variability analysis is from 1982 to 2011.

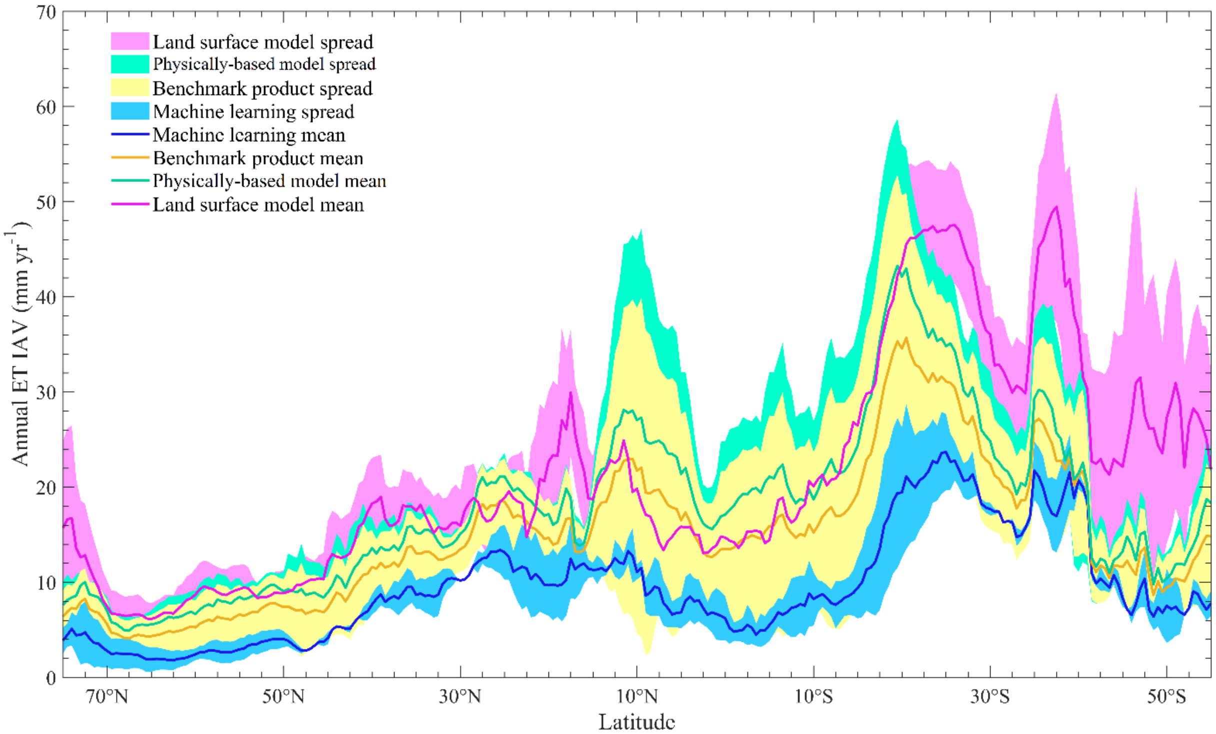

Figure 5. Latitudinal profiles of ET IAV for different categories of models. Each line represents the mean value of the corresponding category and the shading represents the interval of one standard deviation.

3.4 Climatic controls on ET

According to the ensemble remote sensing models, temperature and radiation dominated ET IAV in northern Eurasia, northern and eastern North America, southern China, the Congo River Basin and the southern Amazon River Basin, while precipitation dominated ET IAV in arid regions and semi-arid regions (Fig. 6a). The ensemble machine-learning algorithms had a similar pattern, but suggested a stronger control of radiation in the Amazon Basin and a weaker control of precipitation in several arid regions such as central Asia and northern Australia (Fig. 6b). In comparison, the ensemble LSMs suggested the strongest control of precipitation on ET IAV (Fig. 6). According to the ensemble LSMs, ET IAV was dominated by precipitation IAV in most regions of the Southern Hemisphere and northern low latitudes. Temperature and radiation only controlled northern Eurasia, eastern Canada and part of the Amazon Basin (Fig. 6d). As is shown in Fig. S6, the majority of LSMs agreed on the dominant role of precipitation in controlling ET in regions south of 40ºN. However, the pattern of climatic controls in the ORCHIDEE-MICT model is quite unique and different from all other LSMs. According to the ORCHIDEE-MICT model, radiation and temperature dominate ET IAVs in more regions, and precipitation only controls ET IAVs in eastern Brazil, northern Russia, central Europe and a part of tropical Africa. Since ORCHIDEE-MICT was developed from ORCHIDEE, the dynamic root parameterization in ORCHIDEE-MICT may explain why ET is less driven by precipitation compared to ORCHIDEE (Haverd et al., 2018). It is noted that two machine learning algorithms MTE and RF had significant discrepancies in the spatial pattern of dominant climatic factors. According to the result of MTE, temperature controlled ET IAV in regions north of 45ºN, eastern US, southern China and the Amazon basin (Fig. S6e). By contrast, RF suggested that precipitation and radiation dominated ET IAV in these regions (Fig. S6f).

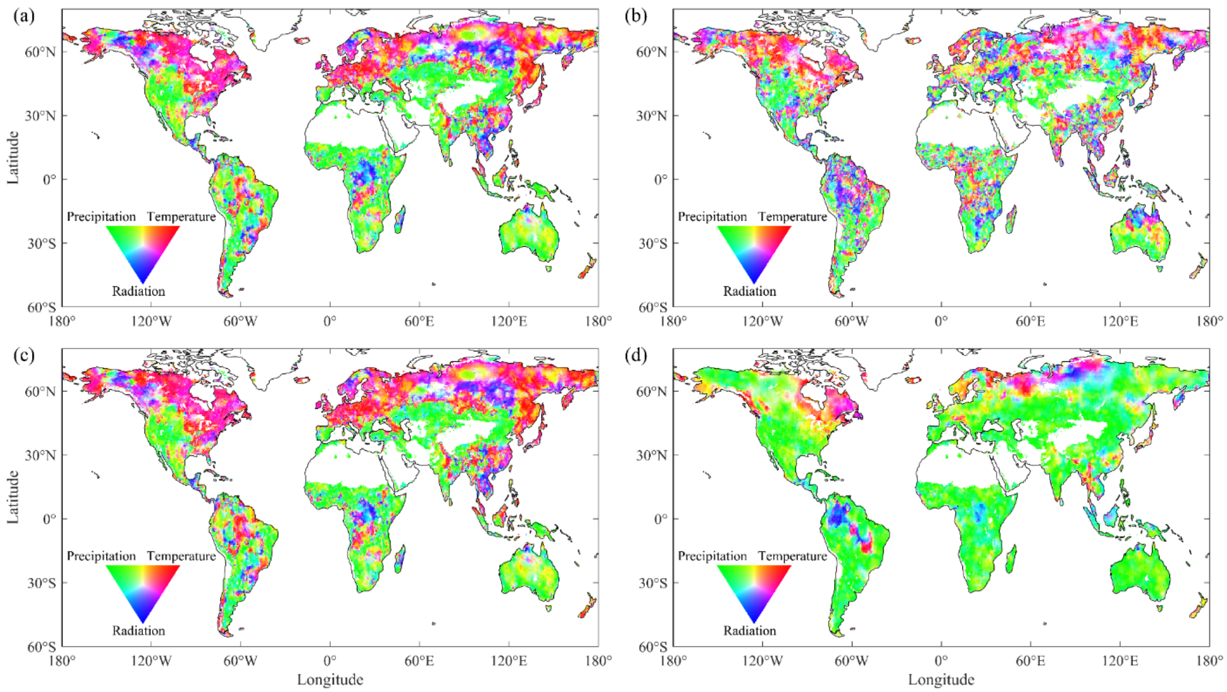

Figure 6. Spatial distributions of climatic controls on inter-annual variation of ET derived from the ensemble means of remote sensing-based physical models (a), machine learning algorithms (b), benchmark data (c), and TRENDY LSMs (d). (red: temperature; green: precipitation; and blue: radiation).

3.5 Long-term trends in global terrestrial ET

All approaches suggested an overall increasing trend in global ET during the period 1982-2011 (Fig. 7), although ET decreased over 1998-2009. This result is consistent with previous studies (Jung et al., 2010; Lian et al., 2018; Zhang et al., 2015). Remote sensing physical models indicated the largest increase in ET (0.62 mm yr^{-2}), followed by the machine-learning method (0.38 mm yr^{-2}), and land surface models (0.23 mm yr^{-2}). Mean ET of all categories except LSMs significantly increased during the study period (p<0.05). It is noted that the ensemble mean ET of different categories are statistically correlated with each other (p<0.001), even if the driving forces of different ET approaches are different.

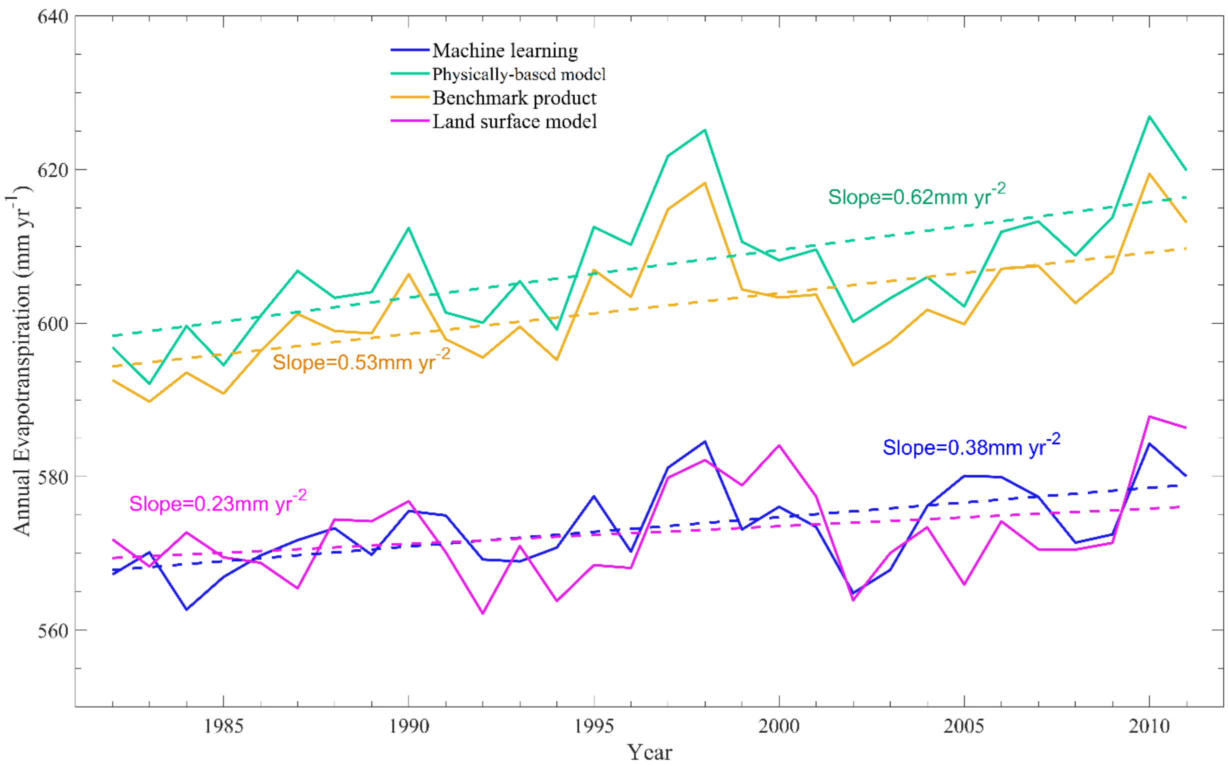

Figure 7. Inter-annual variations in global terrestrial ET estimated by different categories of approaches.

All remote sensing and machine learning estimates indicate a significant positive trend in ET during the study period (p<0.05), although the increase rate of P-LSH (1.07 mm yr^{-2}) is more than three times as large as that of GLEAM (0.33 mm yr^{-2}). Nevertheless, there is a larger discrepancy among LSMs in terms of ET trend. The majority of LSMs (10 of 14) suggest a positive trend with the average trend of 0.34 mm yr^{-2} (p<0.05), and eight of them are statistically significant (see Table 2). However, four LSMs (JSBACH, JULES, ORCHIDEE and ORCHIDEE-MICT) suggest a negative trend with the average trend of -0.12 mm yr^{-2} (p>0.05). Among the four negative trends, only the trend of ORCHIDEE-MICT (−0.34 mm yr^{-2}) is statistically significant (p<0.05).

According to Fig. 8, the ensemble means of all the three approaches showed positive trends of ET over western and southern Africa, western Indian, and northern Australia, and decreasing ET over western United States, southern South America and Mongolia. Discrepancies in ET trends mainly appeared in East Europe, eastern India and central China. LSMs also suggested larger area of decreasing ET in both North America and South America. Although the differences in ET trends among individual models were larger than those among the ensemble means of different approaches, the majority of models agreed that ET increased in western and southern Africa, and decreased in western United States and southern South America (Fig. S2). For both remote sensing estimates and LSMs estimates, ET trends in Amazon Basin had large uncertainty. P-LSH, CLM-45 and VISIT suggested large area of increasing ET, in contrast, GLEAM, JSBACH and ORCHIDEE suggested a large area of decreasing ET.

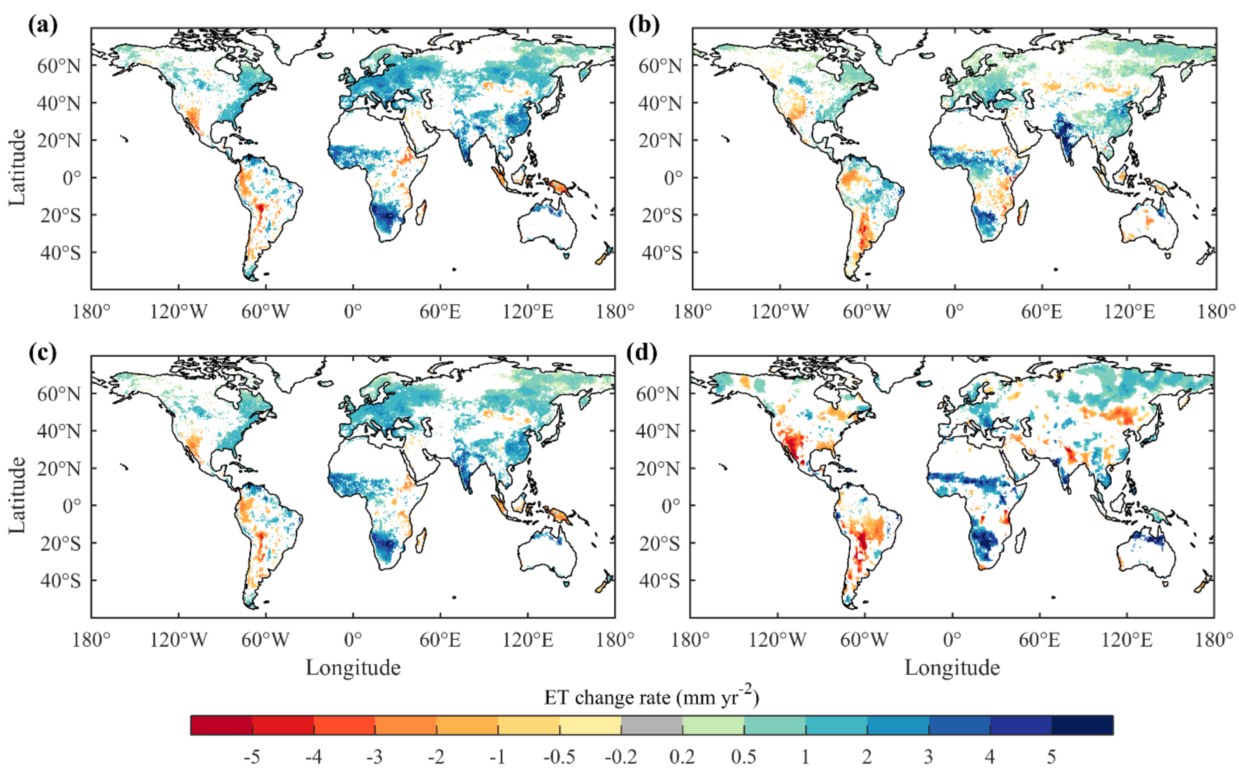

Figure 8. Spatial distributions of ET trends during the period 1982-2011 derived from (a) remote sensing-based physical models, (b) machine learning algorithm, (c) benchmark datasets, and (d) TRENDY LSMs ensemble mean, respectively. Regions with non-significant trends were excluded.

3.6 Impacts of vegetation changes on ET variations

During the period 1982-2011, global LAI trends estimated from remote sensing data and from the ensemble LSMs are 2.51×10^{-3} m^2 m^{-2} yr^{-1} ($p<0.01$) and 4.63×10^{-3} m^2 m^{-2} yr^{-1} ($p<0.01$), respectively (Table 2). All LSMs suggested a significant positive trend in global LAI (greening). It was found that, for both benchmark estimates and LSMs estimates, the spatial pattern of trends in ET matched well with that of trends in LAI (Fig. 8c-d and Fig. S5a-b), indicating significant effects of vegetation dynamics on ET variations. According to the results of multiple linear regression, all models agreed that greening of the Earth since the early 1980s intensified terrestrial ET (Table 2), although there was a significant discrepancy in the magnitude of ET intensification which varied from 0.04 mm yr^{-2} to 0.70 mm yr^{-2}. The ensemble LSMs suggested a smaller ET increase (0.23 mm yr^{-}2) than the ensemble remote sensing physical models (0.62 mm yr^{-2}) and machine-learning algorithm (0.38 mm yr^{-2}). Nevertheless, the greening-induced ET intensification estimated by LSMs (0.37 mm yr^{-2}) is larger than that estimated by remote sensing models (0.28 mm yr^{-2}) and machine-learning algorithms (0.09 mm yr^{-2}) because LSMs suggested a stronger greening trend than remote sensing models. The contribution of vegetation greening to ET intensification estimated by the ensemble LSMs is larger than 100% while the contributions estimated by the ensemble remote sensing physical models (0.62 mm yr^{-2}) and machine-learning algorithm are smaller than 50%. Although TRENDY LSMs were driven by the same climate data and remote sensing physical models were driven by varied climate data, TRENDY LSMs still showed a larger discrepancy in terms of the effect of vegetation greening on terrestrial ET than remote sensing physical models because of the significant differences in both LAI trends (1.74-13.63×10^{-3} m^2 m^{-2} yr^{-1}) and the sensitivities of ET to LAI (4.04-217.39 mm yr^{-2} per m^2 m^{-2}). In comparison, remote sensing physical models had smaller discrepancies in terms of the sensitivity of ET to LAI (55.78-143.43 mm yr^{-2} per m^2 m^{-2}).

4. Discussion and perspectives

4.1 Sources of uncertainty

4.1.1 Uncertainty in the ET estimation of Amazon Basin

LSMs show large discrepancies in the magnitude and trend of ET in the Amazon Basin (Fig. 3 and Fig. S3). However, it is challenging to identify the uncertainty sources. Given that the TRENDY LSMs used uniform meteorological inputs, the discrepancies in ET estimates among the participating models mainly arise from the differences in underlying model structures and parameters. One potential source of uncertainty is the parameterization of root water uptake. In the Amazon Basin, large root depth was confirmed by field measurements (Nepstad et al., 2004). However, many LSMs have an unrealistically small rooting depth (generally less than 2 m), neglecting the existence and significance of deep roots. The incorrect root distributions enlarge the differences in plant available water and root water uptake, producing large uncertainties in ET. In addition, differences in the parameterization of other key processes pertinent to ET such as LAI dynamics (Fig. S5), canopy conductance variations (Table 1), water movements in the soil (Abramopoulos et al., 1988; Clark et al., 2015; Noilhan and Mahfouf, 1996) and soil moisture's control on transpiration (Purdy et al., 2018; Szutu and Papuga, 2019) also increase the uncertainty in ET. The above-mentioned processes are not independent of each other but interact in complex ways to produce the end result.

4.1.2 Uncertainty in the ET estimation of arid and semi-arid regions

In arid and semi-arid regions, benchmark products show much larger differences in the magnitude of ET than LSMs (Fig. S2). One cause of this phenomenon is the difference in meteorological forcing. Remote sensing and machine learning datasets used different forcing data. For precipitation, RF used the CRUNCEPv6 dataset, MTE used the Global Precipitation Climatology Centre (GPCC) dataset, MODIS used the Global Modeling and Assimilation Office (GMAO) dataset, GLEAM used the Multi-Source Weighted-Ensemble Precipitation (MSWEP) dataset, PML-CSIRO used the Princeton Global Forcing (PGF) and the WATCH Forcing Data ERA-Interim (WFDEI) datasets, and P-LSH used data derived from four independent sources. Since precipitation is the key climatic factor controlling ET in arid and semi-arid regions (Fig. 6), discrepancies between different forcing precipitation (Sun et al., 2018) may be the main source of large uncertainty there. In comparison, the uniform forcing data reduced the inter-model range in ET estimates of TRENDY LSMs. Nevertheless, it is noted that the congruence across LSMs ET estimates doesn't necessarily mean they are the correct representation of ET. The narrower inter-model range may suggest shared biases. All remote sensing models and machine learning algorithms except GLEAM do not explicitly take the effects of soil moisture into account (Table S1). Given that soil moisture is pivotal to both canopy conductance and soil evaporation in arid and semi-arid regions (A et al., 2019; De Kauwe et al., 2015; Medlyn et al., 2015; Purdy et al., 2018), the lack of soil moisture information also increases the bias in ET estimation. In addition, the accuracy of remotely-sensing data itself is also an uncertainty source. The retrieval of key land surface variables, such as leaf area index and surface temperature, is influenced by vegetation architecture, solar zenith angle and satellite observational angle, particularly over heterogeneous surface (Norman and Becker, 1995).

4.1.3 Uncertainty in the ET IAV in the Southern Hemisphere

In regions south of 20ºS (including Australia, southern Africa and southern South America), the ET IAVs of remote sensing models and machine learning algorithms are smaller than that of LSMs (Fig. 4 and 5), although their spatial patterns are similar. In these regions, GLEAM, the only remote sensing model that explicitly considers the effects of soil moisture, has larger ET IAVs than other remote sensing models and has similar ET IAVs with LSMs (Fig. S4). This could imply that most existing remote sensing models may underestimate ET IAVs in the Southern Hemisphere because the effects of soil moisture are not explicitly considered. Machine learning algorithms show much smaller IAVs than other models (Fig. 4 and S4). The main reason is that ET inter-annual variability is partly neglected in the training process because the magnitude of ET inter-annual variability is usually smaller than the spatial and seasonal variability (Anav et al., 2015; Jung et al., 2019). Moreover, the IAV of satellite-based key land surface variables such as LAI, fAPAR and surface temperature may be not reliable because of the effects of clouds, which also affects the estimation of IAV of satellite-based ET. It is noted that LSMs ET IAVs show large differences in latitudes south of 20ºS (Fig. 5). This divergence in ET IAV indicates that LSMs need better representation of ET response to climate in the Southern Hemisphere.

4.1.4 Uncertainty in global ET trend

All the three categories of ET models detected an overall positive trend in global terrestrial ET since the early 1980s, which is in agreement with previous studies (Mao et al., 2015; Miralles et al., 2014; Zeng et al., 2018a; Zeng et al., 2018b; Zeng et al., 2014; Zhang et al., 2015; Zhang et al., 2016b). Benchmark products generally suggested stronger ET intensification than LSMs. The weaker ET intensification in LSMs may be induced by the response of stomatal conductance to increasing atmospheric CO_2 concentration. The increasing CO_2 affects ET in two ways. On one hand, increasing CO_2 can effectively reduce stomatal conductance and thus decrease transpiration (Heijmans et al., 2001; Leipprand and Gerten, 2006; Swann et al., 2016); on the other hand, it can increase vegetation productivity and thus increase LAI. For benchmarks, the second effect could be captured by remotely sensed LAI, NDVI or fAPAR, while the first effect was neglected by all models except P-LSH (Zhang et al., 2015). In contrast, both effects were modeled in all TRENDY LSMs.

LAI dynamics have significant influences on ET. The increased LAI trend (greening) since the early 1980s was reported by previous studies (Mao et al., 2016; Zhu et al., 2016) and is also confirmed by remote sensing data and all TRENDY LSMs used in this study (Table 2 and Fig. S5). Zhang et al. (2015) found that the positive trend of global terrestrial ET over 1982-2013 was mainly driven by an increase in LAI and the enhanced atmosphere water demand. Using a land–atmosphere coupled global climate model (GCM), Zeng et al. (2018b) further estimated that global LAI increased about 8%, resulting in an increase of 0.40±0.08 mm yr^{-2} in global ET (contributing to 55%±25% of the ET increase). This number is close to the estimates of ensemble LSMs (0.37±0.18 mm yr^{-2}). In comparison, remote sensing models and machine learning algorithms used in this study suggested smaller greening-induced ET increases. It is noted that TRENDY LSMs still showed a larger discrepancy in terms of the effect of vegetation greening on terrestrial ET than remote sensing physical models (Table 2) because of the significant differences in LAI trend ($1.74\text{-}13.63\times10^{-3}$ m^2 m^{-2} yr^{-1}) and in the sensitivity of ET to LAI (4.04-217.39 mm yr^{-2} per m^2 m^{-2}). Uncertainties in LAI trend may arise from inappropriate carbon allocations and deficits in responding to water deficits (Anav et al., 2013; Hu et al., 2018; Murray-Tortarolo et al., 2013; Restrepo‐Coupe et al., 2017). Additionally, for machine-learning algorithms, the results from insufficient long-term in situ measurements and sparse observations in tropical, boreal and arid regions imply that there likely are deficiencies in representing the temporal variations.

4.1.5 Lack of knowledge of the effects of irrigation

Irrigation accounts for about 90% of human consumptive water use and largely affects ET in irrigated croplands (Siebert et al., 2010). Global water withdrawals for irrigation were estimated to be within the range of 1161-3800 $km^3\ yr^{-1}$ around the year 2000, and largely increased during the period 2000-2014 (Chen et al., 2019). However, none of the remote sensing-based physical models and machine-learning algorithms explicitly accounted for the effects of irrigation on ET, although these effects could be taken into account to some extent by using observed LAI, NDVI, or fAPAR to drive the models (Zhang et al., 2015). Considering that annual ET may surpass annual precipitation in cropland, Zhang et al. (2016b) used the Budyko hydrometeorological model to constrain PML-CSIRO model only in grids covered by non-crop vegetation. But the process of irrigation affecting evaporation was still not taken into consideration. For TRENDY LSMs, only 2 of 14 models (DLEM and ISAM) included the irrigation processes (Le Quéré et al., 2018). Therefore, the effects of irrigation are largely neglected in existing global ET datasets, which reduces the accuracy of local ET estimates in regions with a large proportion of irrigated cropland.

4.1.6 ET variability across precipitation gradient and its planetary boundary

Precipitation is the source of terrestrial evapotranspiration. According to Fig. 9a, the vast majority of models agree that ET has the largest IAV in regions with annual precipitation between 700 mm and 1000 mm, although the magnitude of ET IAV has substantial discrepancies among different models. The low ET IAV in arid and semi-arid regions doesn’t mean ET is stable in these regions. In fact, ET has the largest coefficient of variation (CoV, the ratio of ET standard deviation to ET mean value) in arid regions, and all models show a clear negative trend of CoV with increasing precipitation (Fig. 9b). This is mainly caused by the large CoV of precipitation in arid regions (Fatichi et al., 2012).

In comparison, terrestrial ET shows a much smaller IAV at the global scale (Table 2), ranging from 4.8 to 12.2 mm yr^{-1} (one standard deviation), which only equals to 1.0-1.8% of global annual mean ET. The model results suggest that global terrestrial ET stabilizes at about 6.74×10^4 km^3 yr^{-1} (603 mm yr^{-1}), which is close to previous estimates (Alton et al., 2009; Mueller et al., 2011; Oki and Kanae, 2006; Zeng et al., 2012).The stability of global terrestrial ET is probably based on partitioning the solar constant and suggests that, at a global scale, droughts in one place are balanced by excess rain in other places so it all evens out. It implies that ET also has a potential planetary boundary, a suggestion made by Running (2012) on NPP as a planetary boundary. ET integrates four aspects of the current planetary boundaries defined by Steffen et al. (2015) : climate change, freshwater use, land-system change, and biochemical flows. Given ET's importance in linking terrestrial water, carbon, nutrient and energy cycles, more studies on the ET planetary boundary are needed under the background of intensifying global change and increasing human perturbations on the Earth system.

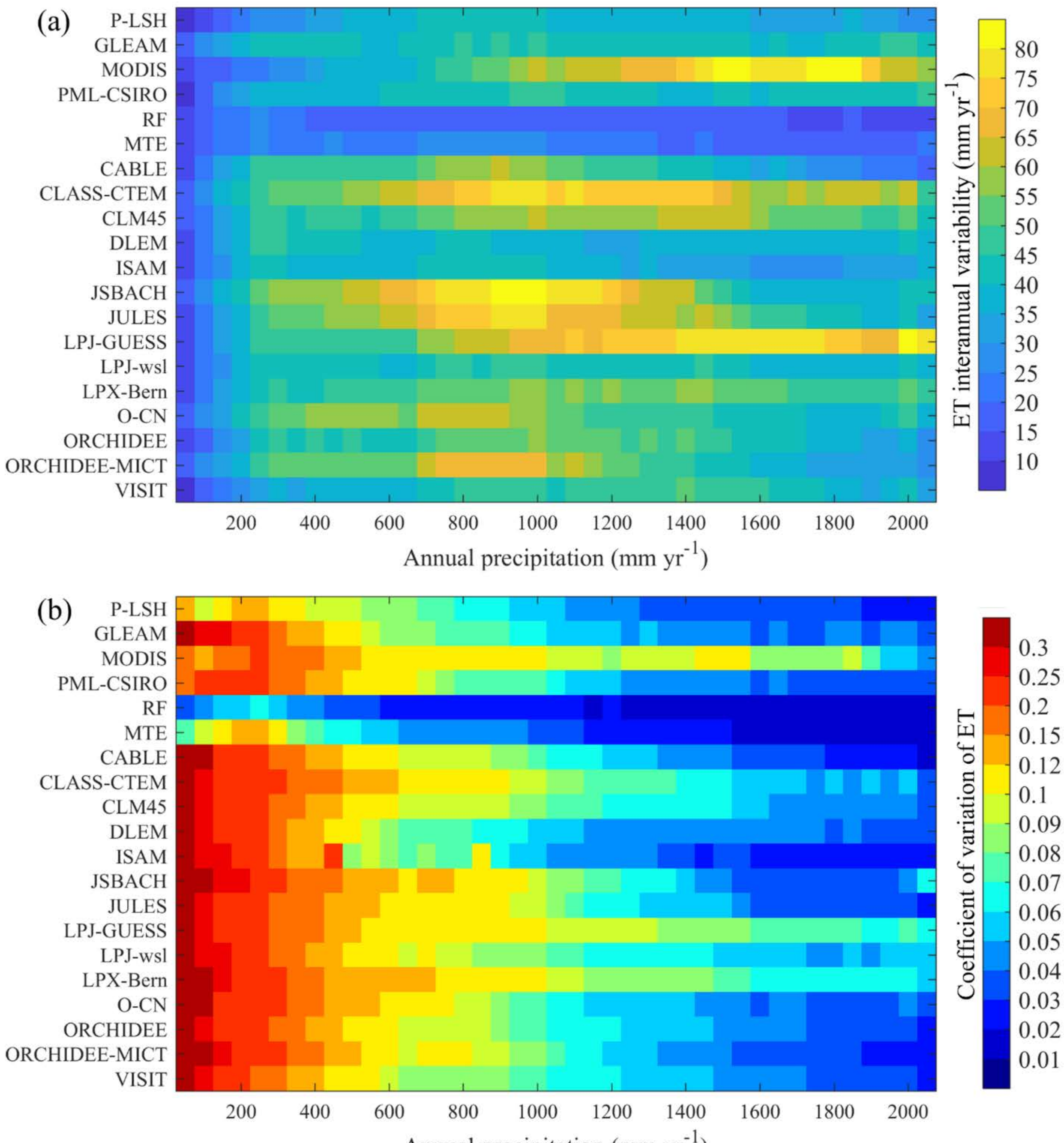

Figure 9. Interannual variability (a) and coefficient of variation (b) of ET in each 50mm interval of mean annual precipitation.

In short, the multi-model inter-comparison indicates that considerable uncertainty exists in both the temporal and spatial variations in global ET estimates, even though a large portion of models adopt similar ET algorithms (Table 1). The major uncertainty source is different for different types of models and regions. The uncertainty is induced by multiple factors, including problems pertinent to parameterization of land processes, lack of in situ measurements, remote sensing acquisition, scaling effects and meteorological forcing. Based on the results of different approaches, we suggest that global terrestrial ET also has a potential planetary boundary, with the value being about 6.74×10^{4} km^{3} yr^{-1} (603 mm yr^{-1}), which is consistent with previous estimates.

4.2 Recommendations for future development

4.2.1 Remote sensing-based physical methods

In the past decades, the development of remote sensing technologies has contributed to the boom of various ET estimating methods. However, there is still a large room for remote sensing technologies to improve (Fisher et al., 2017). Developing new platforms and sensors that have improved global spatiotemporal coverage and using multi-band, multi-source remote sensing data are the key points. Planned or newly launched satellites, such as NASA's GRACE Follow-On (GRACE-FO) mission and ECOsystem Spaceborne Thermal Radiometer Experiment on Space Station (ECOSTRESS) mission, will improve the accuracy of terrestrial ET estimates. ECOSTRESS's thermal infrared (TIR) multispectral scanner is capable of monitoring diurnal temperature patterns at high-resolutions, which gives insights into plant response to water stress and the means to understand sub-daily ET dynamics (Hulley et al.). GRACE Follow-On observations can be used to constrain subsurface lateral water transfers, which helps to correct soil moisture and subsequently improves the accuracy of ET estimates (Rouholahnejad and Martens, 2018). Moreover, building integrated methods that fuse different ET estimates or the upstream satellite-based biophysical variables from different platforms and the other forcing data will be helpful to improve the accuracy and spatiotemporal coverage of ET (Ke et al., 2016; Ma et al., 2018; Semmens et al., 2016).

The theories and retrieval algorithms of ET and related key biophysical variables also need to be further improved. For example, the method for canopy conductance calculation may be improved by integrating remote sensing based solar-induced chlorophyll fluorescence (SIF) data. SIF data in existing Global Ozone Monitoring Experiment-2 (GOME-2), Orbiting Carbon Observatory-2 (OCO-2) and TROPOspheric Monitoring Instrument (TROPOMI) and the forthcoming OCO-3 and Geostationary Carbon Cycle Observatory (GeoCarb) satellites provide a good opportunity for diagnosing transpiration and for ET partitioning at multiple spatiotemporal scales (Pagán et al., 2019; Stoy et al., 2019; Sun et al., 2017). Theoretical advancements in nonequilibrium thermodynamics and Maximum Entropy Production (MEP) could be incorporated into the classical ET theories (Xu et al., 2019; Zhang et al., 2016a). In addition, quantifying the effects of CO_2 fertilization on stomatal conductance is pivotal for remote sensing models to capture the long-term trend of terrestrial ET.

Most existing remote sensing-based ET studies focused on total ET, however, the partitioning of ET between transpiration, soil evaporation, and canopy interception may have significant divergence even though the total ET is accurately estimated (Talsma et al., 2018b). In current remote sensing-based ET models, soil evaporation, which is sensitive to precipitation events and soil moisture, is the part with the largest error (Talsma et al., 2018a). Therefore incorporating the increasing accessible satellite-based precipitation, soil moisture observations and soil property data will contribute to the improvement of soil evaporation estimation. Meanwhile, the consideration of soil evaporation under herbaceous vegetation and canopy will also reduce the errors.

4.2.2 Machine learning methods

It is well known that the capability of machine-learning algorithms in providing accurate ET estimates largely depends on the representativeness of training datasets in describing ecosystem behaviors (Yao et al., 2017). As a result, machine-learning algorithms may not perform well outside the range of the data used for their training. Unfortunately, long-term field observations out of northern temperate regions are still insufficient. This is an important cause of the small spatial gradient and small IAVs of machine-learning ET. Given that remote sensing is capable of providing broad coverage of key biophysical variables at reasonable spatial and temporal resolutions, one way to overcome this challenge is to exclusively use remote sensing observations as training data (Jung et al., 2019; Poon and Kinoshita, 2018). Another simple way to make IAVs of machine-learning ET more realistic is normalizing the yearly anomalies when comparing with ET estimates from LSMs and remote sensing physical models (Jung et al., 2019). New machine-learning techniques, including the extreme learning machine and the adaptive neuro-fuzzy inference system, can be used to improve the accuracy of ET estimation (Gocic et al., 2016; Kişi and Tombul, 2013). The emerging deep learning methods such as recurrent neural network (RNN) and Long Short-Term Memory (LSTM) have large potential to outcompete conventional machine-learning methods in modelling ET time series (Reichstein et al., 2018; Reichstein et al., 2019). Almost all machine-learning datasets used precipitation rather soil moisture as explanatory variable when training. However, soil moisture rather than precipitation directly controls ET. As more and more global remote sensing based soil moisture datasets become available, using soil moisture products as input is expected to improve the accuracy of ET estimates, especially for regions with sparse vegetation coverage (Xu et al., 2018).

4.2.3 Land surface models

In contrast to observation-based methods, LSMs are able to project future changes in ET, and can disentangle the effects of different drivers on ET through factorial analysis. However, results from LSMs are only as good as their parameterizations of complex land surface processes which are limited by our incomplete understanding of physical and biological processes (Niu et al., 2011). Although TRENDY LSMs are the state-of-the-art process-based global land surfaces models, improvements are still needed because several important processes are missing or not being appropriately parameterized. Most of the TRENDY LSMs did not simulate the processes relevant to human management including irrigation (Chen et al., 2019) and application of fertilizers (Mao et al., 2015), and natural disturbances like wildfire (Poon and Kinoshita, 2018). Incorporating these processes into present LSMs is critical, although introduction of new model parameters potentially also leads to an increase in a model's uncertainty.

In light of the importance of soil water availability in constraining canopy conductance and dynamics, accurate representation of hydrological processes is a core task for LSMs, particularly in dry regions. Integrating a dynamic root water uptake function and hydraulic redistribution into the LSM can significantly improve its performance of estimating seasonal ET and soil moisture (Li et al., 2012). Moreover, other hydrological processes including groundwater (Decker, 2015), lateral flow (Rouholahnejad and Martens, 2018) and water vapor diffusion at the soil surface (Chang et al., 2018) need to be simulated and correctly represented to reproduce the dynamics of soil water and ET. Since canopy LAI plays an important role in regulating ET, correctly simulating vegetation dynamics is also critical. One way is to correct the initialization, distribution, and parameterization of vegetation phenology in LSMs (Murray-Tortarolo et al., 2013; Zhang et al., 2019). Appropriate carbon allocation scheme and parameterization of vegetation's response to water deficits are also important for reproducing vegetation dynamics (Anav et al., 2013).

5. Conclusion

In this study, we evaluated twenty global terrestrial ET estimates including four from remote sensing-based physical models, two from machine-learning algorithms and fourteen from TRENDY LSMs. The ensemble mean values of global terrestrial ET for the three categories agreed well, ranging from 589.6 mm yr^{-1} to 617.1 mm yr^{-1}. All the three categories detected an overall positive trend in global ET during the period 1982-2011 and suggested a positive effect of vegetation greening on ET intensification. However, the multi-model inter-comparison indicates that considerable uncertainties still exist in both temporal and spatial variations in global ET estimates. LSMs had significant differences in the ET magnitude in tropical regions especially the Amazon Basin, while benchmark ET products showed larger inter-model range in arid and semi-arid regions than LSMs. Trends in LSMs ET estimates also had significant discrepancies. These uncertainties are induced by parameterization of land processes, meteorological forcing, lack of in situ measurements, remote sensing acquisition and scaling effects. Model developments and observational improvements provide two parallel pathways towards improving the accuracy of global terrestrial ET estimation.

Code and data availability

TRENDYv6 data are available from S.S. (s.a.sitch@exeter.ac.uk) on reasonable request. MODIS ET data are available from http://files.ntsg.umt.edu/data/NTSG_Products/MOD16/. GLEAM ET are available from https://www.gleam.eu/. Both Model Tree Ensemble and Random Forest ET are available from https://www.bgc-jena.mpg.de/geodb/projects/FileDetails.php. P-LSH ET are available from http://files.ntsg.umt.edu/data/ET_global_monthly/Global_8kmResolution/. PML-CSIRO ET are from https://data.csiro.au/dap/landingpage?pid=csiro:17375. CRU-

NCEPv8 data are available from Nicolas Viovy on reasonable request. GIMMS LAI3gV1 data are available from R. B. Myneni on reasonable request. GIMMS NDVI3gV1 data are available from https://ecocast.arc.nasa.gov/data/pub/gimms/3g.v1/.

Author contributions

S.P. initiated this research and was responsible for the integrity of the work as a whole. N.P. carried out the analyses. S.P., N.P., H.T. and H.S. wrote the manuscript with contributions from all authors. P.F., S.S., V.K.A., V.H., A.K.J., E.K., S.L., D.L., J.E.M.S.N., C.O., B.P., H.T. and S.Z. contributed to the TRENDY results.

Competing interests

The authors declare that they have no conflict of interest.

Acknowledgements

This study has been supported partially by grants from National Science Foundation (1903722 and 1243232), AU-OUC Joint Center Program and Auburn University IGP Program. A.K.J. was support in part by Department of Energy (No. DE－SC0016323) and NSF (NSF AGS 12-43071). D.L. acknowledges funding from the National Institute of Food and Agriculture/US Department of Agriculture (2015- 67003-23489 and 2015-67003-23485). S.L. acknowledges support from EC H2020 (CCiCC; grant no 821003) and SNSF (grant no. 20020_172476). V.H. acknowledges support from the Earth Systems and Climate Change Hub, funded by the Australian Government’s National Environmental Science Program. We thank all people who provided data used in this study, in particular, the TRENDY modelling groups. Additional details on funding support for the participating 14 land surface models have been provided in the TRENDY Project.

References

A, Y., Wang, G., Liu, T., Xue, B., and Kuczera, G.: Spatial variation of correlations between vertical soil water and evapotranspiration and their controlling factors in a semi-arid region, Journal of Hydrology, 574, 53-63, 2019.

Abramopoulos, F., Rosenzweig, C., and Choudhury, B.: Improved ground hydrology calculations for global climate models (GCMs): Soil water movement and evapotranspiration, Journal of Climate, 1, 921-941, 1988.

Allen, R. G., Pereira, L. S., Raes, D., and Smith, M.: Crop evapotranspiration-Guidelines for computing crop water requirements-FAO Irrigation and drainage paper 56, Fao, Rome, 300, D05109, 1998.

Alton, P., Fisher, R., Los, S., and Williams, M.: Simulations of global evapotranspiration using semiempirical and mechanistic schemes of plant hydrology, Global biogeochemical cycles, 23, 2009.

Anav, A., Friedlingstein, P., Beer, C., Ciais, P., Harper, A., Jones, C., Murray‐Tortarolo, G., Papale, D., Parazoo, N. C., and Peylin, P.: Spatiotemporal patterns of terrestrial gross primary production: A review, Reviews of Geophysics, 53, 785-818, 2015.

Anav, A., Murray-Tortarolo, G., Friedlingstein, P., Sitch, S., Piao, S., and Zhu, Z.: Evaluation of land surface models in reproducing satellite Derived leaf area index over the high-latitude northern hemisphere. Part II: Earth system models, Remote Sensing, 5, 3637-3661, 2013.

Antonopoulos, V. Z., Gianniou, S. K., and Antonopoulos, A. V.: Artificial neural networks and empirical equations to estimate daily evaporation: application to lake Vegoritis, Greece, Hydrological Sciences Journal, 61, 2590-2599, 2016.

Barman, R., Jain, A. K., and Liang, M.: Climate‐driven uncertainties in modeling terrestrial energy and water fluxes: a site‐level to global‐scale analysis, Global change biology, 20, 1885-1900, 2014.

Bodesheim, P., Jung, M., Gans, F., Mahecha, M. D., and Reichstein, M.: Upscaled diurnal cycles of land–atmosphere fluxes: a new global half-hourly data product, Earth Syst. Sci. Data, 10, 1327-1365, 2018.

Breiman, L.: Random forests, Machine learning, 45, 5-32, 2001.

Chang, L.-L., Dwivedi, R., Knowles, J. F., Fang, Y.-H., Niu, G.-Y., Pelletier, J. D., Rasmussen, C., Durcik, M., Barron-Gafford, G. A., and Meixner, T.: Why Do Large-Scale Land Surface Models Produce a Low Ratio of Transpiration to Evapotranspiration?, Journal of Geophysical Research: Atmospheres, 123, 9109-9130, 2018.

Chen, Y., Feng, X., Fu, B., Shi, W., Yin, L., and Lv, Y.: Recent global cropland water consumption constrained by observations, Water Resources Research, 2019. 2019.

Chen, Y., Xia, J., Liang, S., Feng, J., Fisher, J. B., Li, X., Li, X., Liu, S., Ma, Z., and Miyata, A.: Comparison of satellite-based evapotranspiration models over terrestrial ecosystems in China, Remote Sensing of Environment, 140, 279-293, 2014.

Clark, M. P., Fan, Y., Lawrence, D. M., Adam, J. C., Bolster, D., Gochis, D. J., Hooper, R. P., Kumar, M., Leung, L. R., and Mackay, D. S.: Improving the representation of hydrologic processes in Earth System Models, Water Resources Research, 51, 5929-5956, 2015.

Cleugh, H. A., Leuning, R., Mu, Q., and Running, S. W.: Regional evaporation estimates from flux tower and MODIS satellite data, Remote Sensing of Environment, 106, 285-304, 2007.
d'Orgeval, T., Polcher, J., and Rosnay, P. d.: Sensitivity of the West African hydrological cycle in ORCHIDEE to infiltration processes, Hydrology and Earth System Sciences, 12, 1387-1401, 2008.
Dai, A.: Precipitation characteristics in eighteen coupled climate models, Journal of Climate, 19, 4605-4630, 2006.
De Kauwe, M. G., Kala, J., Lin, Y.-S., Pitman, A. J., Medlyn, B. E., Duursma, R. A., Abramowitz, G., Wang, Y., and Gonzalez Miralles, D.: A test of an optimal stomatal conductance scheme within the CABLE land surface model, Geoscientific Model Development, 8, 431-452, 2015.
Decker, M.: Development and evaluation of a new soil moisture and runoff parameterization for the CABLE LSM including subgrid‐scale processes, Journal of Advances in Modeling Earth Systems, 7, 1788-1809, 2015.
Dou, X. and Yang, Y.: Evapotranspiration estimation using four different machine learning approaches in different terrestrial ecosystems, Computers and Electronics in Agriculture, 148, 95-106, 2018.
Douville, H., Ribes, A., Decharme, B., Alkama, R., and Sheffield, J.: Anthropogenic influence on multidecadal changes in reconstructed global evapotranspiration, Nature Climate Change, 3, 59, 2013.
Famiglietti, J. and Wood, E. F.: Evapotranspiration and runoff from large land areas: Land surface hydrology for atmospheric general circulation models, Surveys in Geophysics, 12, 179-204, 1991.
Fatichi, S., Ivanov, V. Y., and Caporali, E.: Investigating Interannual Variability of Precipitation at the Global Scale: Is There a Connection with Seasonality?, Journal of Climate, 25, 5512-5523, 2012.
Feng, Y., Cui, N., Gong, D., Zhang, Q., and Zhao, L.: Evaluation of random forests and generalized regression neural networks for daily reference evapotranspiration modelling, Agricultural Water Management, 193, 163-173, 2017.
Fisher, J. B., Malhi, Y., Bonal, D., Da Rocha, H. R., De Araujo, A. C., Gamo, M., Goulden, M. L., Hirano, T., Huete, A. R., and Kondo, H.: The land–atmosphere water flux in the tropics, Global Change Biology, 15, 2694-2714, 2009.
Fisher, J. B., Melton, F., Middleton, E., Hain, C., Anderson, M., Allen, R., McCabe, M. F., Hook, S., Baldocchi, D., and Townsend, P. A.: The future of evapotranspiration: Global requirements for ecosystem functioning, carbon and climate feedbacks, agricultural management, and water resources, Water Resources Research, 53, 2618-2626, 2017.
Fisher, J. B., Tu, K. P., and Baldocchi, D. D.: Global estimates of the land–atmosphere water flux based on monthly AVHRR and ISLSCP-II data, validated at 16 FLUXNET sites, Remote Sensing of Environment, 112, 901-919, 2008.
Fu, B. P.: On the calculation of the evaporation from land surface, Sci. Atmos. Sin, 5, 23-31, 1981.
Fu, G., Charles, S. P., and Yu, J.: A critical overview of pan evaporation trends over the last 50 years, Climatic change, 97, 193, 2009.
Gedney, N., Cox, P., Betts, R., Boucher, O., Huntingford, C., and Stott, P.: Detection of a direct carbon dioxide effect in continental river runoff records, Nature, 439, 835, 2006.

Glenn, E. P., Nagler, P. L., and Huete, A. R.: Vegetation index methods for estimating evapotranspiration by remote sensing, Surveys in Geophysics, 31, 531-555, 2010.

Gocic, M., Petković, D., Shamshirband, S., and Kamsin, A.: Comparative analysis of reference evapotranspiration equations modelling by extreme learning machine, Computers and Electronics in Agriculture, 127, 56-63, 2016.

Good, S. P., Noone, D., and Bowen, G.: Hydrologic connectivity constrains partitioning of global terrestrial water fluxes, Science, 349, 175-177, 2015.

Guimberteau, M., Zhu, D., Maignan, F., Huang, Y., Chao, Y., Dantec-Nédélec, S., Ottlé, C., Jornet-Puig, A., Bastos, A., and Laurent, P.: ORCHIDEE-MICT (v8. 4.1), a land surface model for the high latitudes: model description and validation, Geoscientific Model Development, 11, 121, 2018.

Haverd, V., Smith, B., Nieradzik, L., Briggs, P. R., Woodgate, W., Trudinger, C. M., Canadell, J. G., and Cuntz, M.: A new version of the CABLE land surface model (Subversion revision r4601) incorporating land use and land cover change, woody vegetation demography, and a novel optimisation-based approach to plant coordination of photosynthesis, Geosci. Model Dev., 11, 2995-3026, 2018.

Heijmans, M. M., Arp, W. J., and Berendse, F.: Effects of elevated CO2 and vascular plants on evapotranspiration in bog vegetation, Global Change Biology, 7, 817-827, 2001.

Hu, Z., Shi, H., Cheng, K., Wang, Y. P., Piao, S., Li, Y., Zhang, L., Xia, J., Zhou, L., and Yuan, W.: Joint structural and physiological control on the interannual variation in productivity in a temperate grassland: A data - model comparison, Global change biology, 24, 2965-2979, 2018.

Huang, S., Bartlett, P., and Arain, M. A.: Assessing nitrogen controls on carbon, water and energy exchanges in major plant functional types across North America using a carbon and nitrogen coupled ecosystem model, Ecological modelling, 323, 12-27, 2016.

Hulley, G., Hook, S., Fisher, J., and Lee, C.: ECOSTRESS, A NASA Earth-Ventures Instrument for studying links between the water cycle and plant health over the diurnal cycle, 2017 IEEE International Geoscience and Remote Sensing Symposium (IGARSS), 2017, 5494-5496.

Ito, A.: Evaluation of the impacts of defoliation by tropical cyclones on a Japanese forest's carbon budget using flux data and a process - based model, Journal of Geophysical Research: Biogeosciences, 115, 2010.

Jackson, R., Reginato, R., and Idso, S.: Wheat canopy temperature: a practical tool for evaluating water requirements, Water resources research, 13, 651-656, 1977.

Jimenez, C., Prigent, C., Mueller, B., Seneviratne, S. I., McCabe, M., Wood, E., Rossow, W., Balsamo, G., Betts, A., and Dirmeyer, P.: Global intercomparison of 12 land surface heat flux estimates, Journal of Geophysical Research: Atmospheres, 116, 2011.

Jung, M., Koirala, S., Weber, U., Ichii, K., Gans, F., Camps-Valls, G., Papale, D., Schwalm, C., Tramontana, G., and Reichstein, M.: The FLUXCOM ensemble of global land-atmosphere energy fluxes, Scientific Data, 6, 74, 2019.

Jung, M., Reichstein, M., and Bondeau, A.: Towards global empirical upscaling of FLUXNET eddy covariance observations: validation of a model tree ensemble approach using a biosphere model, Biogeosciences, 6, 2001-2013, 2009.

Jung, M., Reichstein, M., Ciais, P., Seneviratne, S. I., Sheffield, J., Goulden, M. L., Bonan, G., Cescatti, A., Chen, J., and De Jeu, R.: Recent decline in the global land evapotranspiration trend due to limited moisture supply, Nature, 467, 951, 2010.

Jung, M., Reichstein, M., Margolis, H. A., Cescatti, A., Richardson, A. D., Arain, M. A., Arneth, A., Bernhofer, C., Bonal, D., and Chen, J.: Global patterns of land ‐ atmosphere fluxes of carbon dioxide, latent heat, and sensible heat derived from eddy covariance, satellite, and meteorological observations, Journal of Geophysical Research: Biogeosciences, 116, 2011.

Jung, M., Reichstein, M., Schwalm, C. R., Huntingford, C., Sitch, S., Ahlström, A., Arneth, A., Camps-Valls, G., Ciais, P., and Friedlingstein, P.: Compensatory water effects link yearly global land CO2 sink changes to temperature, Nature, 541, 516-520, 2017.

Ke, Y., Im, J., Park, S., and Gong, H.: Downscaling of MODIS One kilometer evapotranspiration using Landsat-8 data and machine learning approaches, Remote Sensing, 8, 215, 2016.

Keller, K. M., Lienert, S., Bozbiyik, A., Stocker, T. F., Frank, D. C., Klesse, S., Koven, C. D., Leuenberger, M., Riley, W. J., and Saurer, M.: 20th century changes in carbon isotopes and water-use efficiency: tree-ring-based evaluation of the CLM4. 5 and LPX-Bern models, Biogeosciences (Online), 14, 2017.

Kendall, M. G.: Rank correlation methods, 1955. 1955.

Khan, M. S., Liaqat, U. W., Baik, J., and Choi, M.: Stand-alone uncertainty characterization of GLEAM, GLDAS and MOD16 evapotranspiration products using an extended triple collocation approach, Agricultural and Forest Meteorology, 252, 256-268, 2018.

Kisi, O., Sanikhani, H., Zounemat-Kermani, M., and Niazi, F.: Long-term monthly evapotranspiration modeling by several data-driven methods without climatic data, Computers and Electronics in Agriculture, 115, 66-77, 2015.

Kişi, Ö. and Tombul, M.: Modeling monthly pan evaporations using fuzzy genetic approach, Journal of hydrology, 477, 203-212, 2013.

Knauer, J., Werner, C., and Zaehle, S.: Evaluating stomatal models and their atmospheric drought response in a land surface scheme: A multibiome analysis, Journal of Geophysical Research: Biogeosciences, 120, 1894-1911, 2015.

Lawrence, D. M., Thornton, P. E., Oleson, K. W., and Bonan, G. B.: The partitioning of evapotranspiration into transpiration, soil evaporation, and canopy evaporation in a GCM: Impacts on land–atmosphere interaction, Journal of Hydrometeorology, 8, 862-880, 2007.

Le Quéré, C., Andrew, R. M., Friedlingstein, P., Sitch, S., Pongratz, J., Manning, A. C., Korsbakken, J. I., Peters, G. P., Canadell, J. G., and Jackson, R. B.: Global carbon budget 2017, Earth Syst. Sci. Data, 10, 405-448, 2018.

Leipprand, A. and Gerten, D.: Global effects of doubled atmospheric CO2 content on evapotranspiration, soil moisture and runoff under potential natural vegetation, Hydrological Sciences Journal, 51, 171-185, 2006.

Leuning, R., Zhang, Y., Rajaud, A., Cleugh, H., and Tu, K.: A simple surface conductance model to estimate regional evaporation using MODIS leaf area index and the Penman ‐ Monteith equation, Water Resources Research, 44, 2008.

Li, J., Wang, Y. P., Duan, Q., Lu, X., Pak, B., Wiltshire, A., Robertson, E., and Ziehn, T.: Quantification and attribution of errors in the simulated annual gross primary production and latent heat fluxes by two global land surface models, Journal of Advances in Modeling Earth Systems, 8, 1270-1288, 2016.

Li, L., Wang, Y. P., Yu, Q., Pak, B., Eamus, D., Yan, J., Gorsel, E., and Baker, I. T.: Improving the responses of the Australian community land surface model (CABLE) to seasonal drought, Journal of Geophysical Research: Biogeosciences, 117, 2012.

Li, Z.-L., Tang, R., Wan, Z., Bi, Y., Zhou, C., Tang, B., Yan, G., and Zhang, X.: A review of current methodologies for regional evapotranspiration estimation from remotely sensed data, Sensors, 9, 3801-3853, 2009.
Lian, X., Piao, S., Huntingford, C., Li, Y., Zeng, Z., Wang, X., Ciais, P., McVicar, T. R., Peng, S., and Ottlé, C.: Partitioning global land evapotranspiration using CMIP5 models constrained by observations, Nature Climate Change, 8, 640, 2018.
Liu, M., Tian, H., Chen, G., Ren, W., Zhang, C., and Liu, J.: Effects of Land‐Use and Land‐Cover Change on Evapotranspiration and Water Yield in China During 1900‐2000 1, JAWRA Journal of the American Water Resources Association, 44, 1193-1207, 2008.
Ma, Y., Liu, S., Song, L., Xu, Z., Liu, Y., Xu, T., and Zhu, Z.: Estimation of daily evapotranspiration and irrigation water efficiency at a Landsat-like scale for an arid irrigation area using multi-source remote sensing data, Remote Sensing of Environment, 216, 715-734, 2018.
Mann, H. B.: Nonparametric tests against trend, Econometrica: Journal of the Econometric Society, 1945. 245-259, 1945.
Mao, J., Fu, W., Shi, X., Ricciuto, D. M., Fisher, J. B., Dickinson, R. E., Wei, Y., Shem, W., Piao, S., and Wang, K.: Disentangling climatic and anthropogenic controls on global terrestrial evapotranspiration trends, Environmental Research Letters, 10, 094008, 2015.
Mao, J., Ribes, A., Yan, B., Shi, X., Thornton, P. E., Séférian, R., Ciais, P., Myneni, R. B., Douville, H., and Piao, S.: Human-induced greening of the northern extratropical land surface, Nature Climate Change, 2016. 2016.
Martens, B., Gonzalez Miralles, D., Lievens, H., van der Schalie, R., de Jeu, R. A., Fernández-Prieto, D., Beck, H. E., Dorigo, W., and Verhoest, N.: GLEAM v3: Satellite-based land evaporation and root-zone soil moisture, Geoscientific Model Development, 10, 1903-1925, 2017.
Maselli, F., Papale, D., Chiesi, M., Matteucci, G., Angeli, L., Raschi, A., and Seufert, G.: Operational monitoring of daily evapotranspiration by the combination of MODIS NDVI and ground meteorological data: Application and evaluation in Central Italy, Remote sensing of environment, 152, 279-290, 2014.
Medlyn, B. E., Zaehle, S., De Kauwe, M. G., Walker, A. P., Dietze, M. C., Hanson, P. J., Hickler, T., Jain, A. K., Luo, Y., and Parton, W.: Using ecosystem experiments to improve vegetation models, Nature Climate Change, 5, 528, 2015.
Miralles, D., Holmes, T., De Jeu, R., Gash, J., Meesters, A., and Dolman, A.: Global land-surface evaporation estimated from satellite-based observations, Hydrology and Earth System Sciences, 15, 453-469, 2011.
Miralles, D., Jiménez, C., Jung, M., Michel, D., Ershadi, A., McCabe, M., Hirschi, M., Martens, B., Dolman, A., and Fisher, J.: The WACMOS-ET project-Part 2: Evaluation of global terrestrial evaporation data sets, Hydrology and Earth System Sciences, 20, 823-842, 2016.
Miralles, D., van den Berg, M., Gash, J., Parinussa, R., Jeu, R., Beck, H., Holmes, T., Jimenez, C., Verhoest, N., and Dorigo, W.: El Nino-La Nina cycle and recent trends in continental evaporation, Nature Climate Change, 4, 122-126, 2014.
Monteith, J. L.: Evaporation and environment, 1965, 4.
Mu, Q., Heinsch, F. A., Zhao, M., and Running, S. W.: Development of a global evapotranspiration algorithm based on MODIS and global meteorology data, Remote sensing of Environment, 111, 519-536, 2007.

Mu, Q., Zhao, M., and Running, S. W.: Improvements to a MODIS global terrestrial evapotranspiration algorithm, Remote Sensing of Environment, 115, 1781-1800, 2011.

Mueller, B., Hirschi, M., Jimenez, C., Ciais, P., Dirmeyer, P., Dolman, A., Fisher, J., Jung, M., Ludwig, F., and Maignan, F.: Benchmark products for land evapotranspiration: LandFlux-EVAL multi-data set synthesis, Hydrology and Earth System Sciences, 2013. 2013.

Mueller, B., Seneviratne, S. I., Jimenez, C., Corti, T., Hirschi, M., Balsamo, G., Ciais, P., Dirmeyer, P., Fisher, J., and Guo, Z.: Evaluation of global observations ‐ based evapotranspiration datasets and IPCC AR4 simulations, Geophysical Research Letters, 38, 2011.

Murray-Tortarolo, G., Anav, A., Friedlingstein, P., Sitch, S., Piao, S., Zhu, Z., Poulter, B., Zaehle, S., Ahlström, A., and Lomas, M.: Evaluation of land surface models in reproducing satellite-derived LAI over the high-latitude northern hemisphere. Part I: Uncoupled DGVMs, Remote Sensing, 5, 4819-4838, 2013.

Nagler, P. L., Scott, R. L., Westenburg, C., Cleverly, J. R., Glenn, E. P., and Huete, A. R.: Evapotranspiration on western US rivers estimated using the Enhanced Vegetation Index from MODIS and data from eddy covariance and Bowen ratio flux towers, Remote sensing of environment, 97, 337-351, 2005.

Nepstad, D., Lefebvre, P., Lopes da Silva, U., Tomasella, J., Schlesinger, P., Solórzano, L., Moutinho, P., Ray, D., and Guerreira Benito, J.: Amazon drought and its implications for forest flammability and tree growth: A basin ‐ wide analysis, Global change biology, 10, 704-717, 2004.

Niu, G. Y., Yang, Z. L., Mitchell, K. E., Chen, F., Ek, M. B., Barlage, M., Kumar, A., Manning, K., Niyogi, D., and Rosero, E.: The community Noah land surface model with multiparameterization options (Noah ‐ MP): 1. Model description and evaluation with local ‐ scale measurements, Journal of Geophysical Research: Atmospheres, 116, 2011.

Noilhan, J. and Mahfouf, J.-F.: The ISBA land surface parameterisation scheme, Global and planetary Change, 13, 145-159, 1996.

Norman, J. M. and Becker, F.: Terminology in thermal infrared remote sensing of natural surfaces, Remote Sensing Reviews, 12, 159-173, 1995.

Oki, T. and Kanae, S.: Global hydrological cycles and world water resources, science, 313, 1068-1072, 2006.

Oleson, K. W., Lawrence, D. M., Gordon, B., Flanner, M. G., Kluzek, E., Peter, J., Levis, S., Swenson, S. C., Thornton, E., and Feddema, J.: Technical description of version 4.0 of the Community Land Model (CLM), 2010. 2010.

Pagán, R. B., Maes, H. W., Gentine, P., Martens, B., and Miralles, G. D.: Exploring the Potential of Satellite Solar-Induced Fluorescence to Constrain Global Transpiration Estimates, Remote Sensing, 11, 2019.

Pan, N., Feng, X., Fu, B., Wang, S., Ji, F., and Pan, S.: Increasing global vegetation browning hidden in overall vegetation greening: Insights from time-varying trends, Remote Sensing of Environment, 214, 59-72, 2018a.

Pan, S., Chen, G., Ren, W., Dangal, S. R. S., Banger, K., Yang, J., Tao, B., and Tian, H.: Responses of global terrestrial water use efficiency to climate change and rising atmospheric CO2 concentration in the twenty-first century, International Journal of Digital Earth, 11, 558-582, 2018b.

Pan, S., Tian, H., Dangal, S. R., Yang, Q., Yang, J., Lu, C., Tao, B., Ren, W., and Ouyang, Z.: Responses of global terrestrial evapotranspiration to climate change and increasing atmospheric CO2 in the 21st century, Earth's Future, 3, 15-35, 2015.

Peng, S., Piao, S., Ciais, P., Myneni, R. B., Chen, A., Chevallier, F., Dolman, A. J., Janssens, I. A., Penuelas, J., and Zhang, G.: Asymmetric effects of daytime and night-time warming on Northern Hemisphere vegetation, Nature, 501, 88, 2013.

Peterson, T. C., Golubev, V. S., and Groisman, P. Y.: Evaporation losing its strength, Nature, 377, 687-688, 1995.

Piao, S., Ciais, P., Huang, Y., Shen, Z., Peng, S., Li, J., Zhou, L., Liu, H., Ma, Y., and Ding, Y.: The impacts of climate change on water resources and agriculture in China, Nature, 467, 43-51, 2010.

Poon, P. and Kinoshita, A.: Estimating Evapotranspiration in a Post-Fire Environment Using Remote Sensing and Machine Learning, Remote Sensing, 10, 1728, 2018.

Priestley, C. and Taylor, R.: On the assessment of surface heat flux and evaporation using large-scale parameters, Monthly weather review, 100, 81-92, 1972.

Purdy, A. J., Fisher, J. B., Goulden, M. L., Colliander, A., Halverson, G., Tu, K., and Famiglietti, J. S.: SMAP soil moisture improves global evapotranspiration, Remote Sensing of Environment, 219, 1-14, 2018.

Reichstein, M., Besnard, S., Carvalhais, N., Gans, F., Jung, M., Kraft, B., and Mahecha, M.: Modelling Landsurface Time-Series with Recurrent Neural Nets, IGARSS 2018-2018 IEEE International Geoscience and Remote Sensing Symposium2018, 7640-7643.

Reichstein, M., Camps-Valls, G., Stevens, B., Jung, M., Denzler, J., Carvalhais, N., and Prabhat: Deep learning and process understanding for data-driven Earth system science, Nature, 566, 195-204, 2019.

Restrepo‐Coupe, N., Levine, N. M., Christoffersen, B. O., Albert, L. P., Wu, J., Costa, M. H., Galbraith, D., Imbuzeiro, H., Martins, G., and da Araujo, A. C.: Do dynamic global vegetation models capture the seasonality of carbon fluxes in the Amazon basin? A data‐model intercomparison, Global change biology, 23, 191-208, 2017.

Roderick, M. L. and Farquhar, G. D.: The cause of decreased pan evaporation over the past 50 years, science, 298, 1410-1411, 2002.

Rouholahnejad, E. and Martens, B.: Improving global estimates of terrestrial evaporation by integrating remotely-sensed observations of changes in terrestrial water storage (GRACE) into a global evaporation model (GLEAM), 2018 2018.

Running, S. W.: A measurable planetary boundary for the biosphere, science, 337, 1458-1459, 2012.

Sayemuzzaman, M. and Jha, M. K.: Seasonal and annual precipitation time series trend analysis in North Carolina, United States, Atmospheric Research, 137, 183-194, 2014.

Semmens, K. A., Anderson, M. C., Kustas, W. P., Gao, F., Alfieri, J. G., McKee, L., Prueger, J. H., Hain, C. R., Cammalleri, C., Yang, Y., Xia, T., Sanchez, L., Mar Alsina, M., and Vélez, M.: Monitoring daily evapotranspiration over two California vineyards using Landsat 8 in a multi-sensor data fusion approach, Remote Sensing of Environment, 185, 155-170, 2016.

Sen, P. K.: Estimates of the regression coefficient based on Kendall's tau, Journal of the American statistical association, 63, 1379-1389, 1968.

Shrestha, N. and Shukla, S.: Support vector machine based modeling of evapotranspiration using hydro-climatic variables in a sub-tropical environment, Agricultural and forest meteorology, 200, 172-184, 2015.

Siebert, S., Burke, J., Faures, J.-M., Frenken, K., Hoogeveen, J., Döll, P., and Portmann, F. T.: Groundwater use for irrigation–a global inventory, Hydrology and earth system sciences, 14, 1863-1880, 2010.

Simmons, A., Willett, K., Jones, P., Thorne, P., and Dee, D.: Low‐frequency variations in surface atmospheric humidity, temperature, and precipitation: Inferences from reanalyses and monthly gridded observational data sets, Journal of Geophysical Research: Atmospheres, 115, 2010.

Sitch, S., Smith, B., Prentice, I. C., Arneth, A., Bondeau, A., Cramer, W., Kaplan, J., Levis, S., Lucht, W., and Sykes, M. T.: Evaluation of ecosystem dynamics, plant geography and terrestrial carbon cycling in the LPJ dynamic global vegetation model, Global Change Biology, 9, 161-185, 2003.

Smith, B.: LPJ-GUESS-an ecosystem modelling framework, Department of Physical Geography and Ecosystems Analysis. INES, Sölvegatan, 12, 22362, 2001.

Steffen, W., Richardson, K., Rockström, J., Cornell, S. E., Fetzer, I., Bennett, E. M., Biggs, R., Carpenter, S. R., de Vries, W., de Wit, C. A., Folke, C., Gerten, D., Heinke, J., Mace, G. M., Persson, L. M., Ramanathan, V., Reyers, B., and Sörlin, S.: Planetary boundaries: Guiding human development on a changing planet, Science, 347, 1259855, 2015.

Stoy, P. C., El-Madany, T., Fisher, J. B., Gentine, P., Gerken, T., Good, S. P., Liu, S., Miralles, D. G., Perez-Priego, O., Skaggs, T. H., Wohlfahrt, G., Anderson, R. G., Jung, M., Maes, W. H., Mammarella, I., Mauder, M., Migliavacca, M., Nelson, J. A., Poyatos, R., Reichstein, M., Scott, R. L., and Wolf, S.: Reviews and syntheses: Turning the challenges of partitioning ecosystem evaporation and transpiration into opportunities, Biogeosciences Discuss., 2019, 1-47, 2019.

Sun, Q., Miao, C., Duan, Q., Ashouri, H., Sorooshian, S., and Hsu, K. L.: A review of global precipitation data sets: Data sources, estimation, and intercomparisons, Reviews of Geophysics, 56, 79-107, 2018.

Sun, Y., Frankenberg, C., Wood, J. D., Schimel, D. S., Jung, M., Guanter, L., Drewry, D. T., Verma, M., Porcar-Castell, A., Griffis, T. J., Gu, L., Magney, T. S., Köhler, P., Evans, B., and Yuen, K.: OCO-2 advances photosynthesis observation from space via solar-induced chlorophyll fluorescence, Science, 358, eaam5747, 2017.

Swann, A. L., Hoffman, F. M., Koven, C. D., and Randerson, J. T.: Plant responses to increasing CO2 reduce estimates of climate impacts on drought severity, Proceedings of the National Academy of Sciences, 113, 10019-10024, 2016.

Szutu, D. J. and Papuga, S. A.: Year-Round Transpiration Dynamics Linked With Deep Soil Moisture in a Warm Desert Shrubland, Water Resources Research, 0, 2019.

Tabari, H., Martinez, C., Ezani, A., and Talaee, P. H.: Applicability of support vector machines and adaptive neurofuzzy inference system for modeling potato crop evapotranspiration, Irrigation science, 31, 575-588, 2013.

Talsma, C., Good, S., Miralles, D., Fisher, J., Martens, B., Jimenez, C., and Purdy, A.: Sensitivity of Evapotranspiration Components in Remote Sensing-Based Models, Remote Sensing, 10, 1601, 2018a.

Talsma, C. J., Good, S. P., Jimenez, C., Martens, B., Fisher, J. B., Miralles, D. G., McCabe, M. F., and Purdy, A. J.: Partitioning of evapotranspiration in remote sensing-based models, Agricultural and Forest Meteorology, 260-261, 131-143, 2018b.

Tian, H., Chen, G., Liu, M., Zhang, C., Sun, G., Lu, C., Xu, X., Ren, W., Pan, S., and Chappelka, A.: Model estimates of net primary productivity, evapotranspiration, and water use efficiency in the terrestrial ecosystems of the southern United States during 1895–2007, Forest ecology and management, 259, 1311-1327, 2010.

Trenberth, K. E., Fasullo, J. T., and Kiehl, J.: Earth's global energy budget, Bulletin of the American Meteorological Society, 90, 311-324, 2009.

Vinukollu, R. K., Meynadier, R., Sheffield, J., and Wood, E. F.: Multi‐model, multi‐sensor estimates of global evapotranspiration: Climatology, uncertainties and trends, Hydrological Processes, 25, 3993-4010, 2011a.

Vinukollu, R. K., Wood, E. F., Ferguson, C. R., and Fisher, J. B.: Global estimates of evapotranspiration for climate studies using multi-sensor remote sensing data: Evaluation of three process-based approaches, Remote Sensing of Environment, 115, 801-823, 2011b.

Wang, K. and Dickinson, R. E.: A review of global terrestrial evapotranspiration: Observation, modeling, climatology, and climatic variability, Reviews of Geophysics, 50, 2012.

Wang, K., Dickinson, R. E., Wild, M., and Liang, S.: Evidence for decadal variation in global terrestrial evapotranspiration between 1982 and 2002: 1. Model development, Journal of Geophysical Research: Atmospheres, 115, D20112, 2010.

Wartenburger, R., Seneviratne, S. I., Hirschi, M., Chang, J., Ciais, P., Deryng, D., Elliott, J., Folberth, C., Gosling, S. N., and Gudmundsson, L.: Evapotranspiration simulations in ISIMIP2a-Evaluation of spatio-temporal characteristics with a comprehensive ensemble of independent datasets, Environmental Research Letters, 13, 075001, 2018.

Willett, K. M., Gillett, N. P., Jones, P. D., and Thorne, P. W.: Attribution of observed surface humidity changes to human influence, Nature, 449, 710, 2007.

Xu, D., Agee, E., Wang, J., and Ivanov, V. Y.: Estimation of Evapotranspiration of Amazon Rainforest Using the Maximum Entropy Production Method, Geophysical Research Letters, 0, 2019.

Xu, T., Guo, Z., Liu, S., He, X., Meng, Y., Xu, Z., Xia, Y., Xiao, J., Zhang, Y., Ma, Y., and Song, L.: Evaluating Different Machine Learning Methods for Upscaling Evapotranspiration from Flux Towers to the Regional Scale, Journal of Geophysical Research: Atmospheres, 123, 8674-8690, 2018.

Yao, Y., Liang, S., Cheng, J., Liu, S., Fisher, J. B., Zhang, X., Jia, K., Zhao, X., Qin, Q., and Zhao, B.: MODIS-driven estimation of terrestrial latent heat flux in China based on a modified Priestley–Taylor algorithm, Agricultural and Forest Meteorology, 171, 187-202, 2013.

Yao, Y., Liang, S., Li, X., Chen, J., Liu, S., Jia, K., Zhang, X., Xiao, Z., Fisher, J. B., and Mu, Q.: Improving global terrestrial evapotranspiration estimation using support vector machine by integrating three process-based algorithms, Agricultural and forest meteorology, 242, 55-74, 2017.

Yao, Y., Liang, S., Li, X., Liu, S., Chen, J., Zhang, X., Jia, K., Jiang, B., Xie, X., and Munier, S.: Assessment and simulation of global terrestrial latent heat flux by synthesis of CMIP5 climate models and surface eddy covariance observations, Agricultural and forest meteorology, 223, 151-167, 2016.

Yuan, W., Liu, S., Liu, H., Randerson, J. T., Yu, G., and Tieszen, L. L.: Impacts of precipitation seasonality and ecosystem types on evapotranspiration in the Yukon River Basin, Alaska, Water Resources Research, 46, 2010.

Yue, S., Pilon, P., and Cavadias, G.: Power of the Mann–Kendall and Spearman's rho tests for detecting monotonic trends in hydrological series, Journal of hydrology, 259, 254-271, 2002.

Zaehle, S. and Friend, A.: Carbon and nitrogen cycle dynamics in the O‐CN land surface model: 1. Model description, site‐scale evaluation, and sensitivity to parameter estimates, Global Biogeochemical Cycles, 24, 2010.

Zeng, Z., Peng, L., and Piao, S.: Response of terrestrial evapotranspiration to Earth's greening, Current Opinion in Environmental Sustainability, 33, 9-25, 2018a.

Zeng, Z., Piao, S., Li, L. Z., Wang, T., Ciais, P., Lian, X., Yang, Y., Mao, J., Shi, X., and Myneni, R. B.: Impact of Earth greening on the terrestrial water cycle, Journal of Climate, 31, 2633-2650, 2018b.

Zeng, Z., Piao, S., Lin, X., Yin, G., Peng, S., Ciais, P., and Myneni, R. B.: Global evapotranspiration over the past three decades: estimation based on the water balance equation combined with empirical models, Environmental Research Letters, 7, 014026, 2012.

Zeng, Z., Wang, T., Zhou, F., Ciais, P., Mao, J., Shi, X., and Piao, S.: A worldwide analysis of spatiotemporal changes in water balance‐based evapotranspiration from 1982 to 2009, Journal of Geophysical Research: Atmospheres, 119, 1186-1202, 2014.

Zeng, Z., Zhu, Z., Lian, X., Li, L. Z., Chen, A., He, X., and Piao, S.: Responses of land evapotranspiration to Earth’s greening in CMIP5 Earth System Models, Environmental Research Letters, 11, 104006, 2016.

Zhang, K., Kimball, J. S., Nemani, R. R., and Running, S. W.: A continuous satellite‐derived global record of land surface evapotranspiration from 1983 to 2006, Water Resources Research, 46, 2010.

Zhang, K., Kimball, J. S., Nemani, R. R., Running, S. W., Hong, Y., Gourley, J. J., and Yu, Z.: Vegetation greening and climate change promote multidecadal rises of global land evapotranspiration, Scientific reports, 5, 15956, 2015.

Zhang, K., Kimball, J. S., and Running, S. W.: A review of remote sensing based actual evapotranspiration estimation, Wiley Interdisciplinary Reviews: Water, 3, 834-853, 2016a.

Zhang, L., Lei, H., Shen, H., Cong, Z., Yang, D., and Liu, T.: Evaluating the Representation of Vegetation Phenology in the Community Land Model 4.5 in a Temperate Grassland, Journal of Geophysical Research: Biogeosciences, 124, 187-210, 2019.

Zhang, Y., Peña-Arancibia, J. L., McVicar, T. R., Chiew, F. H., Vaze, J., Liu, C., Lu, X., Zheng, H., Wang, Y., and Liu, Y. Y.: Multi-decadal trends in global terrestrial evapotranspiration and its components, Scientific reports, 6, 19124, 2016b.

Zhu, Z., Bi, J., Pan, Y., Ganguly, S., Anav, A., Xu, L., Samanta, A., Piao, S., Nemani, R. R., and Myneni, R. B.: Global data sets of vegetation leaf area index (LAI) 3g and Fraction of Photosynthetically Active Radiation (FPAR) 3g derived from Global Inventory Modeling and Mapping Studies (GIMMS) Normalized Difference Vegetation Index (NDVI3g) for the period 1981 to 2011, Remote Sensing, 5, 927-948, 2013.

Zhu, Z., Piao, S., Myneni, R. B., Huang, M., Zeng, Z., Canadell, J. G., Ciais, P., Sitch, S., Friedlingstein, P., and Arneth, A.: Greening of the Earth and its drivers, Nature Climate Change, 2016. 2016.

Table 1. Descriptions of models used in this study, including their drivers, adopted algorithms, key equations, limitations and references

Name	Input	Algorithm	Spatial resolution	Temporal resolution	Key equations	Limitations	References

MTE	Climate: precipitation, temperature, sunshine hour, relative humidity, wet days Vegetation: fAPAR	TRIAL ERROR	+ 0.5º×0.5º	Monthly	No specific equation	Insufficient flux observations in tropical regions; with no CO2 effect	Jung et al. (2011)
RF	enhanced vegetation index, fAPAR, leaf area index, land surface temperature, radiation, potential radiation, index of water availability, relative humidity	Randomized decision tree	0.5º×0.5º	Half-hourly	No specific equation	The same with MTE	Bodesheim et al. (2018)
P-LSH	Climate: radiation, air temperature, vapor pressure, wind speed, CO2 Vegetation: AVHRR NDVI	Modified Penman–Monteith	0.083 º×0.083º	Monthly	$E_v = \frac{\Delta R_n + \rho C_p VPD g_a}{\lambda_v(\Delta + \Upsilon\left(1 + \frac{g_a}{g_s}\right))}$ $E_s = RH^{\frac{VPD}{k}} \frac{\Delta R_n + \rho C_p VPD g_a}{\lambda_v(\Delta + \Upsilon\left(1 + \frac{g_a}{g_s}\right))}$	Advantages: more robust physical basis; consider the effects of CO_2 Limitations: high meteorological forcing requirements; canopy conductance is based on proxies;	Zhang et al. (2015)
GLEAM	Climate: precipitation, net radiation, surface soil moisture, land surface temperature, air temperature, snow depth Vegetation: vegetation optical depth	Modified Priestley–Taylor	0.25º×0.25º	Daily	$E_s = f_s S_s \alpha_s \frac{\Delta}{\lambda_v \rho_w(\Delta + \gamma)}(R_n^s - G_s)$ $E_{sc} = f_{sc} S_{sc} \alpha_{sc} \frac{\Delta}{\lambda_v \rho_w(\Delta + \gamma)}(R_n^{sc} - G_{sc})$ $E_{tc} = f_{tc} S_{tc} \alpha_{tc} \frac{\Delta}{\lambda_v \rho_w(\Delta + \gamma)}(R_n^{tc} - G_{tc}) - \beta E_i$	Advantages: simple; low requirement for meteorological data; well-suited for remote sensing observable variables; soil moisture is considered Limitations: many simplifications of physical processes; neither VPD nor surface and aerodynamic resistances are explicitly accounted for; strong dependency on net radiation	(Miralles et al., 2011)
MODIS	Climate: air temperature, shortwave radiation, wind speed, relative humidity, air pressure Vegetation: LAI, fAPAR, albedo	Penman–Monteith–Leuning	0.05 º×0.05 º	Monthly	$E_i = f_{wet} f_c \frac{\Delta(R_n - G) + \rho c_p \frac{VPD}{r_a^{wc}}}{\lambda_v \rho_w(\Delta + \gamma \frac{r_s^{wc}}{r_a^{wc}})}$ $E_v = (1 - f_{wet}) f_c \frac{\Delta(R_n - G) + \rho c_p \frac{VPD}{r_a^t}}{\lambda_v \rho_w(\Delta + \Upsilon \frac{r_s^t}{r_a^t})}$ $E_s = [f_{wet} + \frac{(1 - f_{wet}) h VPD}{\beta}] \frac{(s A_{soil} + \frac{\rho c_p (1 - f_c) VPD}{r_{as}})}{\lambda_v \rho_w(S + \gamma \frac{r_{tot}}{r_{as}})}$	Advantages: more robust physical basis; Limitations: require many variables that are difficult to observe or not observable with satellites; canopy conductance is based on proxies; do not consider soil moisture but use atmospheric humidity as a surrogate; do not	Mu et al. (2011)

						consider the effects of CO_2	
PML-CSIRO	Climate: precipitation, air temperature, vapor pressure, shortwave radiation, longwave radiation, wind speed Vegetation: AVHRR LAI, emissivity and albedo	Penman–Monteith–Leuning	0.5°×0.5°	Monthly	$E_v = \frac{\Delta R_n + \rho C_p VPD g_a}{\lambda_v(\Delta + \Upsilon\left(1 + \frac{g_a}{g_s}\right))}$ $E_s = \frac{f\Delta A_s}{\Delta + \gamma}$ E_i: an adapted version of Gash rainfall interception model (Van et al., 2001)	Advantages: more robust physical basis (compared to Priestley–Taylor equation); biophysically based estimation of surface conductance Limitations: high meteorological forcing requirements; canopy conductance is based on proxies; do not consider the effects of CO_2	Zhang et al. (2016b)

TRENDY LSMs

Advantages: land surface models are process-oriented and physically-based. Given their structure almost all models are capable to allow factorial analysis, where one forcing can be applied at a time. Most models also consider the physiological effect of CO_2 on stomatal closure.

Disadvantages: most models typically do not allow integration/assimilation of observation-based vegetation characteristics. Model parameterizations remain uncertain and a same process is modelled in different ways across models. Model parameters may or may not be physically-based and therefore measurable in the field.

Models participating in the TRENDYv6 comparison were forced by precipitation, air temperature, specific humidity, shortwave radiation, longwave radiation, wind speed based on the CRU-NCEPv8 data as explained in Le Quere et al. 2018. It is very difficult to list all key equations for all land surface models. Here, we just list the stomatal conductance equation for each model.

Name	Algorithm	Spatial resolution	Temporal resolution	Key equations	References
CABLE	Penman-Monteith	0.5°×0.5°	Monthly	$g_s = g_0 + \frac{g_1 f_w A}{c_a - c_p}(1 + \frac{VPD}{VPD_0})^{-1}$	Haverd et al. (2018)
CLASS-CTEM	Modified Penman–Monteith	2.8125°×2.8125 °	Monthly	$g_c = m\frac{A_n p}{(c_s - \Gamma)}\frac{1}{(1 + VPD/VPD_0)} + b\ LAI$	Melton and Arora (2016)
CLM45	Modified Penman–Monteith	1.875 °×2.5 °	Monthly	$g_s = g_0 + \frac{g_1 A}{c_a} RH$	Oleson et al. (2010)
DLEM	Penman–Monteith	0.5°×0.5°	Monthly	$g_s = \max(g_{smax} r_{corr} bf(ppdf) f(T_{min}) f(VPD) f(CO_2), g_{smin})$	Pan et al. (2015)
ISAM	Modified Penman–Monteith	0.5°×0.5°	Monthly	$g_s = m\frac{A}{C_s/P_{atm}} \times \frac{e_s}{e_i} + b_t\beta_t$	Barman et al. (2014)
JSBACH	Penman–Monteith	1.9 °×1.9 °	Monthly	$g_s = \beta_w \frac{1.6A_{n,pot}}{c_a - c_{i,pot}}$	Knauer et al. (2015)
JULES	Penman–Monteith	2.5 °×3.75 °	Monthly	Bare soil conductance: $g_{soil} = \frac{1}{100}(\frac{\theta_1}{\theta_c})^2$ Stomatal conductance is calculated by solving the two equations: $A_l = g_s(C_s - C_i)/1.6$; $\frac{C_i - \Gamma^*}{C_c - \Gamma^*} = f_0(1 - \frac{\Delta}{q_c})$	Li et al. (2016)
LPJ-GUESS	Equations proposed by Monteith (1995)	0.5°×0.5°	Monthly	$g_s = g_{smin} + \frac{1.6A_{dt}}{c_a(1 - \lambda_c)}$	Smith (2001)
LPJ-wsl	Priestley-Taylor	0.5°×0.5°	Monthly	$g_s = g_{smin} + \frac{1.6A_{dt}}{c_a(1 - \lambda_c)}$	Sitch et al. (2003)
LPX-Bern	Modified equation of Monteith (1995)	1°×1°	Monthly	$g_s = g_{smin} + \frac{1.6A_{dt}}{c_a(1 - \lambda_c)}$	Keller et al. (2017)
O-CN	Modified Penman-Monteith	1°×1°	Monthly	$g_s = g_{smin} + \frac{1.6A_{dt}}{c_a(1 - \lambda_c)}$	Zaehle and Friend (2010)

ORCHIDEE	Modified Penman-Monteith	0.5º×0.5º	Monthly	$g_s = g_0 + \frac{A + R_d}{c_a - c_p} f_{vpd}$ g_{soil}= exp(8.206-4.255W/W_{sat})	d'Orgeval et al. (2008)
ORCHIDEE-MICT	Modified Penman-Monteith	0.5º×0.5º	Monthly	$g_s = g_0 + \frac{A + R_d}{c_a - c_p} f_{vpd}$	Guimberteau et al. (2018)
VISIT	Penman–Monteith	0.5º×0.5º	Monthly	$g_s = g_0 + \frac{g_1 f_w A}{c_a - c_p}(1 + \frac{VPD}{VPD_0})^{-1}$	Ito (2010)

Notes: A: net assimilation rate; A_{dt}: total daytime net photosynthesis; $A_{n,pot}$: unstressed net assimilation rate; b: soil moisture factor; b_t: stomatal conductance intercept; c_a: atmospheric CO_2 concentration; c_c: critical CO_2 concentration; c_i: internal leaf concentration of CO_2; $c_{i, pot}$: internal leaf concentration of CO_2 for unstressed conditions; c_s: leaf surface CO_2 concentration; c_p: CO_2 compensation point; e_s: vapor pressure at leaf surface; e_i: saturation vapor pressure inside the leaf; E_s: soil evaporation; E_c: canopy evapotranspiration; E_{dry}: dry canopy evapotranspiration; E_{wet}: wet canopy evapotranspiration; E_v: canopy transpiration; E_i: canopy interception; E_{tc}: transpiration from tall canopy; E_{sc}: transpiration from short canopy; f: fraction of *P* to equilibrium soil evaporation; f_s: soil fraction; f_{sc}: short canopy fraction; f_{tc}: tall canopy fraction; f_{vpd}: factor of the effect of leaf-to-air vapor pressure difference; f_w: a function describing the soil water stress on stomatal conductance; f_{wet}: relative surface wetness parameter; f_0: the maximum ratio of internal to external CO_2; *f(ppdf)*:limiting factor of photosynthetic photo flux density; $f(T_{min})$: limiting factor of daily minimum temperature; *f(VPD)*: limiting factor of vapor pressure deficit; $f(CO_2)$: limiting factor of carbon dioxide; G: ground energy flux; g_a: aerodynamic conductance; g_m: empiricalparameter; g_s: stomatal conductance; g_{smax}: maximum stomatal conductance; g_{smin}: minimum stomatal conductance; g_{soil}: bare soil conductance; g_0: residual stomatal conductance when the net assimilation rate is 0 ; g_1: sensitivity of stomatal conductance to assimilation, ambient CO_2 concentration and environmental controls; I: tall canopy interception loss; m: stomatal conductance slope; P_{atm}: atmospheric pressure; PE_s: potential soil evaporation; PE_{canopy}: potential canopy evaporation; q_a: specific air humidity; q_c: critical humidity deficit; q_s: specific humidity of saturated air; r_a: aerodynamic resistance; r_s: stomatal resistance; R_n: net radiation; Rd: day respiration; RH: relative humidity; T_s: actual surface temperature; VPD: vapor pressure deficit; VPD_0: the sensitivity of stomatal conductance to VPD; W: top soil moisture; W_{canopy}: canopy water; W_{sat}: soil porosity; α: Priestley-Taylor coefficient; α_m: empirical parameter; *β:* a constant accounting for the times in which vegetation is wet; β_t: soil water availability factor between 0 and 1; β_w: A scaling factor to account for water stress; β_s: moisture availability function; ρ: air density; *γ*: psychrometric constant; λ_v: latent heat of vaporization; λ_c: ratio of intercellular to ambient partial pressure of CO_2; r_{corr}: correction factor of temperature and air pressure on conductance; Γ^*: CO_2 compensation point when leaf day respiration is zero; θ_1: parameter of moisture concentration in the top soil layer; θ_c: parameter of moisture concentration in the spatially varying critical soil moisture; Δ: slope of the vapor pressure curve.

Table 2. Inter-annual variability (IAV, denoted as standard deviation) and trend of global terrestrial ET during 1982-2011 and the contribution of vegetation greening to ET trend. * suggests significance of the trend at the 95% confidence level (p<0.05).

	Model	ET IAV (mm yr^{-1})	ET Trend (mm yr^{-2})	Greening-induced ET change (mm yr^{-2})	Sensitivity of ET to LAI (mm yr^{-2} per m^2 m^{-2})	LAI trend (10^{-3} m^2 m^{-2} yr^{-1})
Machine learning	MTE	5.93	0.38*	0.09	35.86	2.51*
RS models	P-LSH	9.95	1.07*	0.34	135.46	2.51*
	GLEAM	8.47	0.33*	0.14	55.78	2.51*
	PML-CSIRO	7.18	0.41*	0.36	143.43	2.51*
	RS model mean	7.98	0.62*	0.28	111.55	2.51*
LSMs	CABLE	9.63	0.07	0.35	102.64	3.41*
	CLASS-CTEM	12.22	0.35*	0.53	134.52	3.94*
	CLM45	8.68	0.38*	0.31	67.54	4.59*
	DLEM	7.21	0.26*	0.53	200.76	2.64*
	ISAM	7.50	0.22	0.16	32.26	4.96*
	JSBACH	10.12	-0.05	0.50	217.39	2.30*
	JULES	11.33	-0.02	0.34	85.21	3.99*
	LPJ-GUESS	7.48	0.50*	0.28	160.92	1.74*
	LPJ-wsl	4.77	0.24*	0.19	31.56	6.02*
	LXP-Bern	4.80	0.20*	0.04	4.04	9.90*
	O-CN	10.41	0.32*	0.53	89.23	5.94*
	ORCHIDEE	9.28	-0.17	0.21	96.33	2.18*
	ORCHIDEE-MICT	10.70	-0.34*	0.50	171.23	2.92*
	VISIT	6.31	0.87*	0.70	51.40	13.62*
	LSM mean	7.73	0.23	0.37	79.91	4.63*